

High-speed acoustic holography with arbitrary scattering objects

Ryuji Hirayama,^{1*} Giorgos Christopoulos,¹ Diego Martinez Plasencia,¹ Sriram Subramanian¹

¹Department of Computer Science, University College London, UK

*Corresponding author. Email: r.hirayama@ucl.ac.uk

Recent advances in high-speed acoustic holography have enabled levitation-based volumetric displays with tactile and audio sensations. However, current approaches do not compute sound scattering of objects' surfaces; thus, any physical object inside can distort the sound field. Here, we present a new technique that allows high-speed multi-point levitation even with arbitrary sound-scattering surfaces and demonstrate a volumetric display that works in the presence of any physical object. Our technique has a two-step scattering model and a simplified levitation solver, which together can achieve over 10,000 updates per second to create volumetric images above and below static sound-scattering objects. The model estimates transducer contributions in real-time by reformulating the boundary element method for acoustic holography, and the solver creates multiple levitation traps. We explain how our technique achieves its speed with minimum loss in the trap quality and illustrate how it brings digital and physical content together by demonstrating new interactive applications.

Introduction

Acoustic levitation (1), a technique that utilizes mechanical energy of sound to levitate and manipulate materials, has been significantly advanced over the last decade through the introduction of two fundamental techniques: phased arrays of transducers (PATs) (2, 3) and acoustic holography (4–6). PATs allow dynamic control of dense arrays of sound sources (e.g., 16×16 ultrasound transducers) while holography, a wavefront-handling technique originally developed in optics, enabled PATs to accurately control sound fields in 3D space. Thanks to its capability of levitating almost any type of materials, acoustic holography using PATs has many potential applications in laboratory-on-chip (7), biology (8), computational fabrication (9), and mid-air displays (6, 10–16). Acoustic levitation is also emerging as a strong candidate for creating new mixed-reality (MR) interfaces that can seamlessly blend the digital and physical worlds, as envisioned in the Ultimate Display of Ivan Sutherland (17).

In general, acoustic holography using PATs relies on a linear model (15, 18, 19), represented by using a transmission matrix F . The matrix F describes how complex activations of N transducers ($\tau \in \mathbb{C}^N$) contribute to the complex acoustic pressures at L points of interest in a sound field ($\zeta \in \mathbb{C}^L$), using a linear system: $\zeta = F\tau$, with $L \ll N$. Each element of this matrix ($F_{l,n}$) is equal to the pressure at the l -th point of interest generated by the n -th transducer when its activation is 1 (i.e., the maximum amplitude with a phase delay of 0 rad), and it can be approximated as a piston model (20) if we consider only direct contributions. Using this common linear model, existing approaches use different solvers to obtain the transducers' activations τ that generate an ideal sound field ζ , which, for example, creates focal points to provide tactile sensations (21, 22) or provides the maximum trapping stiffness (i.e., the Laplacian of the Gor'kov potential, commonly been used as a metric to assess how strong each acoustic trap is (4, 6, 15)) for levitating particles at desired positions (4). One critical milestone in this solving process for acoustic levitation was the introduction of the holographic acoustic element (HAE) framework, which simplified the computation of levitation traps by encoding them as the combination of a holographic acoustic lens creating focal points and a fixed levitation signature (4). This framework supports a huge range of symmetric transducer arrangements (e.g., single-sided, top-bottom, V-shape) and has been extended to multi-point levitation (6). Recent algorithmic advances have further accelerated the computational speed of this framework, and consequently, the accelerated update rates (i.e., 10,000 fps) have enabled PATs to create volumetric visual content (i.e., high-speed levitation) in mid-air using the persistence of vision (POV) effect, together with tactile and audio sensations in order to provide multi-modal experiences (13, 15).

However, realizing the full potential of such approaches is hindered by the model used, which operates under the assumption of empty space. That is, sound scattering of objects' surfaces is not taken into account; thus, any physical object within the working volume can distort the sound field and cause particles to fall.

Transmission matrices F only capture direct contribution from each transducer to each point, ignoring interactions with any sound-scattering objects and implicitly representing an empty working volume. The only objects permitted within the working volume are acoustically transparent materials, which are carefully chosen not to affect sound fields (12), along with the levitated particles, which are usually much smaller than the acoustic wavelength (e.g., $\lambda = 8.65$ mm in this study) and thus can be considered as acoustically transparent as well. To date, there have been limited explorations of acoustically manipulated particles

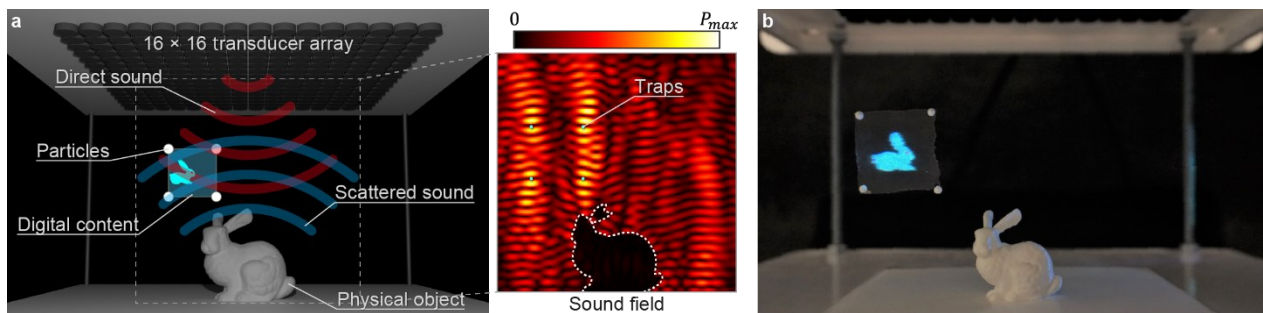
52 in a presence of sound-scattering objects. For example, in one set of papers, the authors explored 2D plane manipulation above flat
53 reflector (2, 6, 19, 23), while in another approach the authors used PATs with acoustic metamaterials to demonstrate a single-
54 particle levitation above a cloaked object (24).

55 Models such as the boundary element method (BEM (25, 26)) can simulate sound-scattering fields, and BEM has been used to
56 levitate objects several times larger than the wavelength (27) or to assemble nanoparticles inside arbitrary shaped closed reservoirs
57 (28, 29). However, BEM is usually considered incompatible with real-time applications, particularly for high demands of POV
58 display applications (i.e., 10,000 fps), and no dynamic manipulation using BEM has been demonstrated in those existing works.

59 To make full use of acoustic holography in more flexible environments, we require a new acoustic holographic technique that
60 does not rely on the assumption of the empty working volume and works in the presence of arbitrary sound-scattering objects. The
61 main challenge in developing such techniques is that the entire process of both *modeling* the transmission matrix and *solving*
62 for transducer phases must be computed in real time for practical applications of particle manipulation (e.g., 50 fps to manipulate
63 particles at 1 cm/s with a step size of 0.2 mm). This becomes even more challenging in order to create volumetric images using the
64 POV effect (13, 15), as these require update rates above 10,000 fps. Thus, producing models as computationally efficient as
65 transmission matrices, but with BEM's power to capture sound-scattering hence becomes the first obvious challenge.

66 For solvers, on the other hand, the HAE framework does not account for sound scattering and thus cannot provide the
67 optimum solutions within the non-empty working volume (i.e., the top array with reflector, see Fig. 1). Therefore, to develop a
68 high-performance solver without the HAE framework, we need more efficient metrics to assess trap quality, compared to the most
69 common current metric given by trapping stiffness (i.e., Laplacian of Gor'kov potential (4, 6)).

70 Here, we present a novel high-performance approach to modeling the extended transmission matrix and solving for transducer
71 phases. Our technique has two novel computational components: a two-step scattering model and a simplified levitation solver. In
72 these components, physical phenomena (i.e., sound scattering, acoustic levitation) are rebuilt or simplified as models that are
73 suitable to be computed at high update rates. We start by reformulating BEM to pre-compute the contribution of each transducer to
74 the mesh and then use these pre-computed values in updating the transmission matrix in real time as the trap positions move. This
75 extended version of the transmission matrix keeps the efficiency of the empty-volume methods but provides the accuracy that is
76 exactly equivalent to BEM. Additionally, we show that a simplified Gor'kov potential can be used as a new metric in our solver
77 instead of stiffness, further improving the computational speed with negligible loss of accuracy. Our approach allows high-speed
78 and accurate multi-point acoustic manipulation, even with arbitrary sound-scattering objects (see Fig. 1 and Movie S1). It allows
79 the creation of volumetric POV images with arbitrarily shaped objects in the working volume by creating levitation traps at high
80 computational rates. Our technique provides extra freedom in system design and allows previously impractical application
81 scenarios, which inherently involve physical objects in their working space, such as mid-air MR displays (see Fig. 1b) and
82 contactless manufacturing. Additionally, thanks to the high computational rates, the displayed content can be interactive to user
83 inputs (e.g., keyboard, hand gestures) in real time. We illustrate for the first time how our acoustic holographic technique brings
84 digital and physical content together by demonstrating several MR applications, such as a mid-air screen, a point-scanning-based
85 volumetric display, and a surface-scanning-based volumetric display. We are the first to demonstrate a free-space surface-
86 scanning-based volumetric display that can create full volumetric images in mid-air, within a non-empty working volume.



87 **Fig. 1. Real-time acoustic holography with arbitrary scattering surfaces.** (a) Schematic concept of our acoustic holographic
88 technique that can create multiple levitation traps in a presence of sound-scattering physical objects. P_{max} represents the maximum
89 amplitude of the pressure in the sound field. (b) Experimental example of our technique that can levitate four particles with a
90 projection screen (i.e., a piece of light fabric), demonstrating a mixed-reality display that creates digital content in the presence of
91 a 3D-printed physical object. The high computational rates of our approach enable the digital content to be interactive to user
92 inputs (i.e., the levitated screen moves according to the keyboard input).
93

94 Results

95 Model and Solver

96 First, we show how our new model and solver realized high-speed multi-point levitation with minimum loss of accuracy, even
97 within a non-empty working volume.

98 *Two-step scattering model:* BEM can model sound scattering objects by modeling them as a mesh of M boundary elements
99 (i.e., we use meshes with 3,000–6,000 elements in our examples). A transmission matrix \mathbf{E} that captures both the direct and
100 scattering contributions of the transducers to target points could be computed by repeating the BEM computation for each of the N
101 single transducers (i.e., $N = 256$). However, each BEM computation involves solving a large dense linear equation system, and
102 therefore, repeating this process for every transducer in real time is not practical. Thus, we propose a new technique to reformulate
103 BEM for acoustic holography to define the matrix \mathbf{E} using three matrices as: $\mathbf{E} = \mathbf{F} + \mathbf{GH}$ (see Fig. 2a). Here, the matrices \mathbf{F} and
104 \mathbf{G} represent the respective contributions from the transducers and mesh elements to the points of interest (i.e., thus, \mathbf{F} is the

conventional transmission matrix capturing only direct contributions), and the matrix \mathbf{H} represents the contribution from the transducers to the mesh elements. The sizes of these matrices are $L \times N$ for \mathbf{E} and \mathbf{F} , $L \times M$ for \mathbf{G} , and $M \times N$ for \mathbf{H} . Given the fact that the inequality $L \ll N \ll M$ is usually satisfied in acoustic levitation, the determination of \mathbf{H} is more time-consuming than the other matrices.

For static set-ups, \mathbf{H} is constant and we can thus pre-compute it once the set-up is defined (i.e., position and normal of each transducer and position, area and normal of each mesh element in the reflector). In contrast, computing \mathbf{F} and \mathbf{G} requires the positions of points of interest in addition to the set-up information. For interactive applications, these points of interest are usually unknown beforehand, and thus \mathbf{F} and \mathbf{G} need to be created in real time depending on the application logic and/or user input. While \mathbf{H} must be pre-computed, computation of \mathbf{F} and \mathbf{G} is highly parallelizable, and our model can achieve high computational rates for this modeling process by using a graphics processing unit (GPU) even in the presence of static sound-scattering objects. Fig. S6a shows the computational speed of only this modeling process after the pre-computation part. Note here that our model is exactly equivalent to BEM, not relying on any approximation to compute the acoustic pressures on the meshes, and thus can be used to model any geometry of scattering objects without sacrifice in accuracy, unlike the methods based on the Rayleigh integral (18, 19, 30), which are limited to flat or slightly curved reflectors. We also note that our model does not require high sampling resolution for 3D models' mesh (i.e., the best-balanced mesh size is $\lambda/2$, see *Mesh-size Dependency of the Trap Quality* and Fig. S7). We also discuss how to adapt our approach to dynamically changing meshes later in *Discussion*.

Simplified levitation solver: We propose a simplified solver using the model above. Our *SIMPLIFIED* solver uses a gradient descent minimizing a simplified metric U' at every trap position $\mathbf{r}_j = (x_j, y_j, z_j)$, allowing us to create multiple stable traps at high computational speed. Our metric U' is based on the Gor'kov potential U , which can be used to compute the acoustic radiation force \mathbf{F}^{rad} applied on a small particle (i.e., much smaller than the acoustic wavelength) at the point j as: $\mathbf{F}^{rad} = -\nabla U(\mathbf{r}_j)$. Here, $U(\mathbf{r}_j)$ can be determined by the complex acoustic pressure p and its spatial derivatives at the trap position \mathbf{r}_j and constant values (K_1 and K_2) as (31):

$$U(\mathbf{r}_j) = K_1 |p|^2 - K_2 \left(\left| \frac{\partial p}{\partial x} \right|^2 + \left| \frac{\partial p}{\partial y} \right|^2 + \left| \frac{\partial p}{\partial z} \right|^2 \right). \quad (1)$$

Trapping stiffness (4, 6) is a common metric to evaluate (and optimize) the quality of acoustic traps and is computed as the Laplacian of the Gor'kov potential ($\nabla^2 U$) at the point j . A traditional method is to create levitation traps by maximizing such trapping stiffness at the desired locations, with an optimization algorithm such as gradient descent (4). However, computing stiffness $\nabla^2 U(\mathbf{r}_j)$ requires sampling pressure values at many points of interest around each trap and thus is computationally heavy for use in real-time applications.

In this study, we accelerate our solving process of creating J traps by using a simplified Gor'kov potential $U'(\mathbf{r}_j)$ as a new metric (i.e., our cost function in gradient descent):

$$U'(\mathbf{r}_j) = K_1 |p|^2 - K_2 \left| \frac{\partial p}{\partial z} \right|^2. \quad (2)$$

The advantage of this new metric is that it can be computed by sampling pressure values at only two points per trap (i.e., the number of total points of interest is $L = 2J$). This simplified metric is suitable for our experimental set-ups, in which the transducers face downward (i.e., $-z$ direction) and sound-scattering objects are placed underneath (see Fig. 1a), allowing them to create standing-wave-like acoustic traps along the z -axis, similar to the commonly-used top-bottom set-ups (6).

Our simplification in Eq. 2 approximates sufficiently the potential $U(\mathbf{r}_j)$ because the derivative of the pressure along the z -axis is more dominant than the derivatives along the other axes. Also, the Gor'kov potential along the z -axis behaves locally as a sinusoidal pattern (32). Thus, the second derivative of such sinusoidal pattern (i.e., trapping stiffness) should also be sinusoidal of opposite sign, supporting our assumption that a negative relationship between $U(\mathbf{r}_j)$ and its Laplacian ($\nabla^2 U(\mathbf{r}_j)$) still holds. Figure 2b validates this, showing the relationship between our new metric and trapping stiffness in our set-ups with a very good correlation (i.e., $R^2 = 0.940$) and experimentally evaluating our assumption. Note here that our simplified metric (Eq. 2) could not be directly used in set-ups, where this assumption is not valid, but this can be easily adjusted to other set-ups such as single-sided, top-bottom, and V-shape, as shown in the section *Metric validity* and Figs. S4.

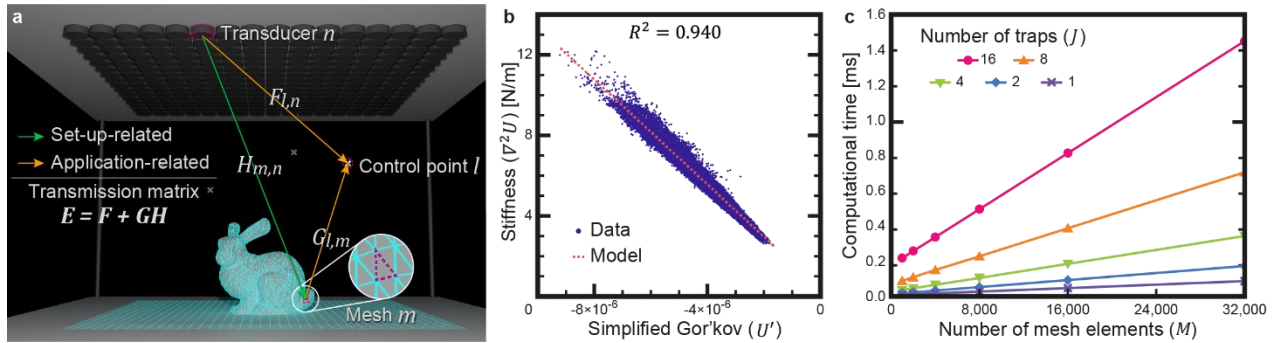
Validation and Performance Evaluation

To evaluate our *SIMPLIFIED* solver in terms of trapping stiffness, we compared it with the other two solvers, which we refer to as *BASELINE* and *HEURISTIC*. The *BASELINE* solver is a traditional method that uses a physically accurate and broadly accepted metric (i.e., trapping stiffness $\nabla^2 U(\mathbf{r}_j)$) to optimize trapping quality (4) but is slow. The *HEURISTIC* solver is an extension of the HAE framework, enabling us to create traps by creating two focal points around each trap with a π -radian offset in the target phases (6). Although this approach is fast and would work well in a single-point manipulation, destructive interference between traps is likely to occur in multi-point manipulation (15). Note here that all the three solvers use our two-step scattering model.

As shown in Fig. S9, our *SIMPLIFIED* solver avoids destructive interference between multiple traps when compared to the *HEURISTIC* solver, while achieving similar quality (i.e., trapping stiffness) than the *BASELINE* solver that directly maximized $\nabla^2 U(\mathbf{r}_j)$ (see *Comparison between the Solvers* for more detailed evaluations). Additionally, with an appropriate initialization, our *SIMPLIFIED* solver can converge within 100 iterations (see *Convergence and Initialization* and Fig. S8). Therefore, our solver represents solutions being the most balanced, realizing accurate and fast acoustic manipulation.

Figure 2c summarizes the computational performance of our acoustic holographic technique. We evaluated how the numbers of traps (J) and mesh elements (M) influence the computational speed. Here, the number of transducers (N) and the number of iterations (K) in the solver were fixed (i.e., $N = 256$, $K = 100$). The results show the linear relationship between them as expected, and high update rates over 10,000 fps (i.e., less than 0.1 ms computational time) can be achieved in several scenarios (e.g., $J = 4$ with $M = \sim 8,000$). For example, the 3D model of the bunny and the flat reflector (i.e., $12 \times 12 \text{ cm}^2$), which was used in the four-trap application in Fig. 1b, is composed of 4,134 elements in total, achieving over 15,000 fps. The plots also show that even with the slowest scenario in the plots (i.e., $J = 16$ and $M = 32,000$), we can still get over 700 fps, which is enough to

167 manipulate particles in real time. Although the set-up-related part cannot be computed in real-time (see *Computational*
 168 *Performance*), this part can be pre-computed once the set-up is defined.

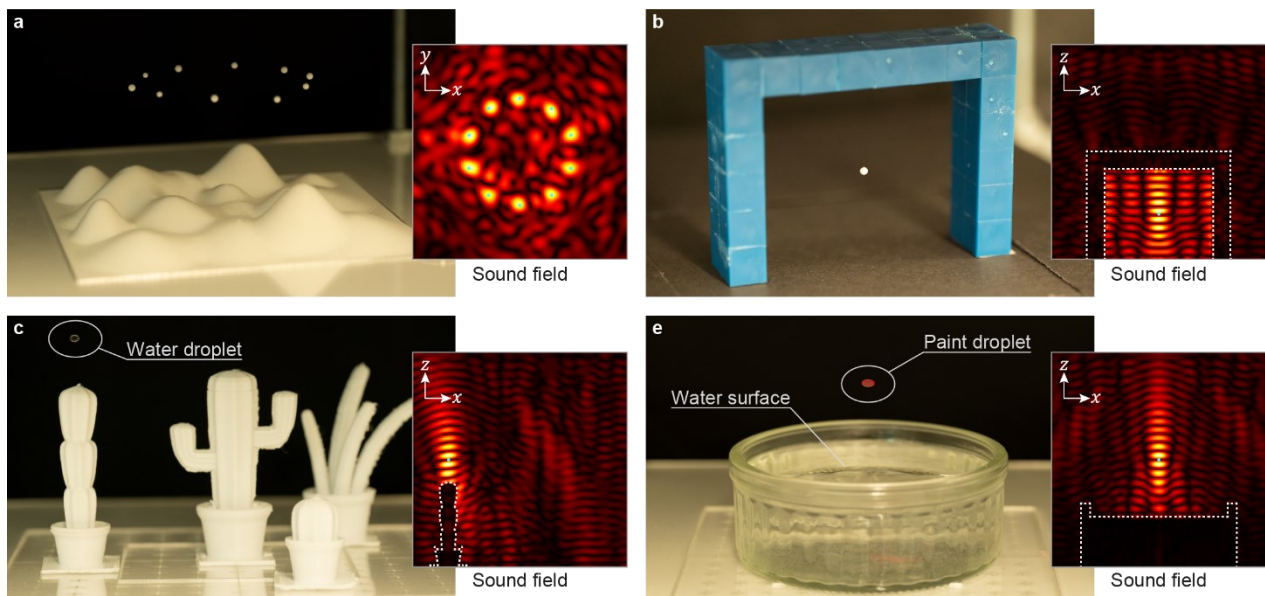


169
 170 **Fig. 2. Performance of the proposed technique.** (a) Schematic explanation of our *two-step* scattering model, adapting
 171 the boundary element method (BEM). (b) Correlation between trapping stiffness $\nabla^2 U$ and the simplified form of the
 172 Gor'kov potential U' , justifying the use of U' as our metric. (c) Computational performance of our acoustic holographic
 173 technique after pre-computation, depending on the numbers of mesh elements (M) and traps (J).

174 **Versatile Manipulation Capabilities**

175 The combination of our two-step scattering model and the simplified levitation solver allows real-time manipulation of materials
 176 in 3D space, in the presence of sound-scattering objects. Figure 3a shows an experimental example of levitating 10 expanded
 177 polystyrene (EPS) particles above a 3D-printed smooth surface. The simulated sound field in the xy -plane $\lambda/4$ above the trap
 178 positions (i.e., the inserted image in Fig. 3a) shows 10 high-pressure points. The closest previous demonstrations (2, 6, 19, 23) of
 179 this example were limited to 2D plane manipulation of EPS particles or liquid droplets just above flat reflector surfaces without
 180 any scattering object. In our case, we have enabled acoustic 3D manipulation even with a non-flat reflector. In addition, particles
 181 can be levitated under sound scattering obstacles, which occlude most direct sound contributions from the transducers (see Fig.
 182 3b), showing manipulation capabilities in scenarios that were not previously possible.

183 Unlike other levitation techniques such as electromagnetics, the acoustic approach can levitate almost any type of material,
 184 including solids and liquids (1). Figure 3c shows the manipulation of a water droplet in the presence of 3D-printed cacti. Acoustic
 185 manipulation of liquid droplets is particularly challenging, as the acoustic velocity of air particles at the trap position needs to be
 186 carefully adjusted, keeping it within the range determined by the droplet's radius and surface tension to avoid droplet atomization
 187 (2, 33). The fast computational rates of our technique enable us to estimate the acoustic velocity in real time, dynamically
 188 adjusting the transducers' amplitudes to make the acoustic velocity constant along the manipulation path (see Fig. S12).
 189 Additionally, by modulating the amplitudes of all the transducers at certain frequencies, we can induce oscillatory vibrations to
 190 levitated droplets, which is useful for mixing multiple materials in a contactless manner without any cross-contamination (34).
 191 Furthermore, our scattering model works even if the scattering surfaces are liquids. Figure 3d shows the manipulation of a mixture
 192 of water droplets, taking into account the liquid surface of a container filled with water (see also Movie S2). We approximated the
 193 liquid surface is acoustically rigid (i.e., $\beta_m = 0$), still showing correct droplet manipulation. Such material independence lends
 194 versatility to our technique, which can be applied in fields such as computational fabrication, laboratory-on-a-chip, and biomedical
 195 imaging. The use of other β_m values is also possible, as detailed in *Two-step Scattering Model*.



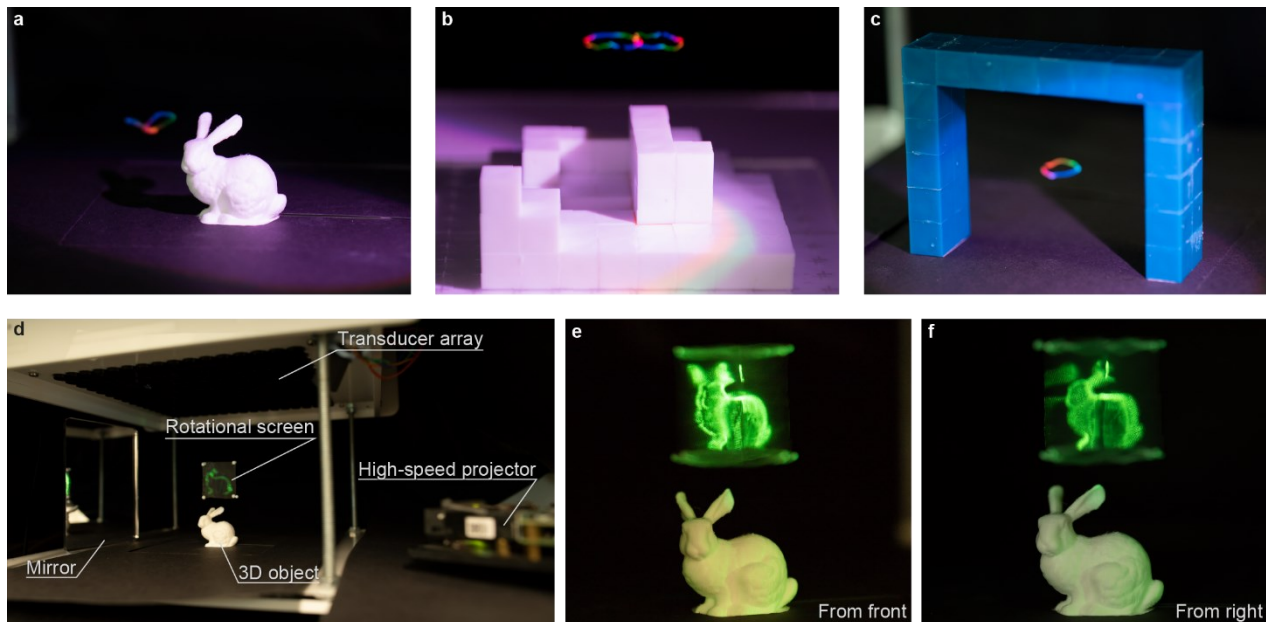
196
 197 **Fig. 3. Levitation capabilities of the proposed technique.** (a) Our technique can create and manipulate multiple traps
 198 individually (i.e., there are 10 traps in the photograph). (b) Traps can be created even under sound-scattering obstacles by

199 utilizing scattered waves. **(c)** Materials that can be manipulated in mid-air include both solids and liquids (i.e., a water
200 droplet is levitated). **(d)** Our scattering model works on scattering surfaces of liquids as well. The inserted boxes show
201 simulated sound fields in the xy -plane $\lambda/4$ above the trap positions for (a) and the xz -plane on the trap positions for the
202 others (b-d), normalized using the maximum amplitude. The white dashed lines in these figures represent the positions of
203 the scattering objects in the planes.

204 **Creation of POV Images Using High Update Rates**

205 An important aspect of our technique is its computational speed. As discussed in the literature (13, 15), high update rates for
206 PATs, of ideally more than 10,000 fps, enable us to manipulate EPS particles at fast velocities (i.e., maximum velocity of 8.75 m/s
207 with the top-bottom setup was reported in (13)), allowing the creation of mid-air volumetric images using the POV effect by
208 scanning particles in 0.1 s (35). The fast computational speeds of our technique (see Fig. 2c) allow such a point-scanning-based
209 method to create volumetric POV images even in the presence of sound-scattering objects. Additionally, thanks to the high update
210 rates of our approach, created POV images can be interactive to user inputs (e.g., keyboard, hand gestures) in real time. Figure 4a
211 shows the creation of a butterfly flapping around a 3D-printed bunny ($M = 4,134$), which can be controlled by hand gestures (see
212 Movie S4), by using a single particle colored by full-color LEDs. Other examples of volumetric shapes are shown in Fig. 4b (see
213 also Movie S3), showing two particles on top of plastic bricks ($M = 5,010$), while Fig. 4c shows a single particle under sound-
214 scattering obstacles ($M = 3,792$). These are the first demonstration of the creation of digital volumetric images with physical
215 objects as a new MR human-computer interface, blurring the boundary between the digital and physical worlds.

216 However, the volumetric geometries that the point-scanning-based approach can create are limited to simple shapes, as
217 demonstrated in Figs 4a, 4b, and 4c, because particles must scan all the geometries in the POV time (i.e., 0.1 s). Therefore, here we
218 additionally demonstrate for the first time a free-space surface-scanning-based display within a non-empty working volume,
219 to create more complex volumetric shapes with many voxels (volume elements). In this approach, we levitated a piece of light fabric
220 with the same levitation set-up used for the point-scanning approach and used a high-speed projector (i.e., 1,440 fps) and a mirror,
221 as shown in Fig. 4d. Our technique can rotate the fabric in the presence of sound-scattering objects at five rotations per second
222 while synchronously projecting cross-sectional images of a 3D model on the rotating fabric, revealing the full volumetric image in
223 mid-air due to the POV effect. The reason we used the mirror is to project images even when the projection direction and the
224 fabric are in parallel. The two photographs taken from the different perspectives (see Figs. 4e and 4f) show the digital 3D image of
225 a bunny projected onto the rotational fabric. The digital 3D image was created on top of a physical bunny ($M = 4,134$), which was
226 3D-printed using the same 3D model for the digital bunny. We can confirm that our system can project complex volumetric shapes
227 in mid-air, which can be viewed from any direction.



228 **Fig. 4. Mixed-reality applications using high-speed acoustic holography. (a, b)** Examples of the creation of volumetric
229 POV images using single and multiple particles with sound-scattering objects. **(c)** POV images can be created even under
230 sound-scattering obstacles. **(d)** Full-volumetric projection of 3D digital content together with a 3D printed object using a
231 quickly rotating screen (i.e., five rotations per second) and a high-speed projector. **(e, f)** Two photographs taken from two
232 different perspectives (i.e., from front and right) to demonstrate full volumetric projection. Note here that the digital and
233 physical objects both used the same 3D model (i.e., bunny) with the same orientation.
234

235 **Discussion**

236 Prior to this work, 3D manipulations of materials using acoustic holography have been accomplished only in an empty volume.
237 This limitation has so far forced the technology to be used in limited scenarios (i.e., no scattering objects around). Here, we
238 overcome this limitation by reformulating and simplifying the model and solver for acoustic holography. Our approach extends the
239 possibilities of acoustic levitation, enabling 3D printing for contactless manufacturing and mixing of physical and digital artifacts
240 for novel MR applications. In this study, we assumed only sound-scattering objects with high acoustic impedance compared to air

241 (e.g., plastic, water), within a single propagation medium (i.e., air). However, BEM can also be used to compute sound scattering
 242 from sound soft boundaries, even through multiple media. The same two-step approach could be applied to such more complex
 243 scenarios, accelerating computational speed and paving the way for real-time exploitation beyond the environments demonstrated.

244 This range of potential scenarios will also increase as we relax our current limitation of using only static scattering objects
 245 (i.e., a single pre-computed matrix \mathbf{H}), but so do the challenges that need to be considered. That is, by removing the need for an
 246 empty volume, our current method already enables ultrasound-based solutions to be applied to many more real-world settings,
 247 such as inside appliances or in the dashboard of a car.

248 An obvious step to support dynamic (i.e., moving/changing) objects would be to pre-compute different \mathbf{H} matrices, one per
 249 state of the object. This would require us to know in advance the nature of the dynamic evolution of the object, but even this
 250 simple step would be enough to enable many novel applications such as 3D printing and contactless assembly, as in all these cases
 251 the evolution of the geometry is known ahead of time.

252 Moving towards fully interactive scenarios opens new challenges and possibilities. For objects interactively changing position
 253 and orientation but with fixed shape, the LU decomposition technique discussed in *Moving Sound-scattering Objects* and Fig. S10
 254 could allow matrix \mathbf{H} to be computed in real-time. The most challenging scenario is when the objects change their shapes,
 255 positions, and orientations in an unpredictable manner (e.g., an MR application where users' hands interact inside the working
 256 volume). New approaches to compute \mathbf{H} in real time would be required here, but one potential solution is to exploit the local
 257 nature of changes. That is, if the positions and/or geometries of objects do not change drastically between updates, the solution for
 258 the previous geometry can be used as good initial estimations for the next geometry, reducing the computational cost. It is worth
 259 noting that the computational rates for this set-up-related part do not need to achieve 10,000 fps, and more conventional rates
 260 could suffice (e.g., >30 fps).

261 Also, our two-step scattering model can be adapted to various PAT arrangements (e.g., top-bottom, V-shape, single-sided; see
 262 Figs. S4d, S4e, S4f) with no modification. This offers great flexibility in designing new applications using our acoustic
 263 holographic technique. However, we need to note that the simplified metric should not be used as in Eq. 2 by default, but rather be
 264 adjusted to the geometric relationship between the involved PATs and trap positions (see Figs. S4a, S4b, S4c). This suggests that
 265 dynamically tuning the most suitable metric simplification for the set-up and content used would enable us to always bring the best
 266 accuracy and speed out of the device.

267 The point-scanning-based approach has been adopted and explored to realize free-space volumetric displays by using several
 268 levitation techniques such as acoustic (13–15), photophoretic (36), and electromagnetic traps (37). In this study, we for the first
 269 time introduced the surface-scanning-based approach into these levitation techniques and achieved the free-space volumetric
 270 display that can represent more voxels with minimum constraint in voxel arrangement, compared to the point-based ones (detailed
 271 in *Surface-scanning-based Volumetric Display*). In comparison with the volumetric displays using mechanically-rotated screens or
 272 emitters (38, 39), the advantage of our approach is that we can manipulate the rotational screen itself within the space that the user
 273 can directly access, highlighting the MR aspect of the acoustic holographic technique proposed in this study.

274 **Materials and Methods**

275 **Modeling sound-scattering for acoustic holography**

276 Our scattering model is based on BEM (25, 26). Therefore, we first describe how the conventional BEM works for general
 277 scattering problems and then how we reformulated BEM for acoustic holography in two steps, to achieve the high update rates.

278 **Conventional BEM for Scattering Problems:** In BEM, acoustic pressure at some point \mathbf{x} can be represented as a boundary
 279 integral equation (i.e., Helmholtz-Kirchhoff integral equation) obtained via Green's theorem. In scattering problems, BEM can be
 280 computed by discretizing the surface of the scattering objects into M mesh elements. The size of the elements is small enough so
 281 that the pressure across each mesh p_m can be considered as constant across the element. Then, under certain impedance boundary
 282 conditions parametrized by β_m , the complex pressure $p(\mathbf{x})$ in the domain of propagation (i.e., the region in which the wave
 283 propagates) is given by the direct incident contributions $p^{inc}(\mathbf{x})$ and scattered contributions from every mesh element as:

$$284 \quad p(\mathbf{x}) = p^{inc}(\mathbf{x}) + \sum_{m=1}^M p_m s_m \left[ik\beta_m G(\mathbf{x}_m, \mathbf{x}) + \frac{\partial G(\mathbf{x}_m, \mathbf{x})}{\partial n(\mathbf{x}_m)} \right]. \quad (3)$$

285 Here, s_m represents the surface area; k is the wavenumber; and β_m denotes the relative surface admittance at the boundary,
 286 computed as the ratio of acoustic impedances of the propagation medium Z_0 and the scattering object Z_s (i.e., $\beta_m = Z_0/Z_s$; $\beta_m =$
 287 0 when the surface is acoustically rigid). $G(\mathbf{y}, \mathbf{x})$ is the so-called free-field Green's function, defined in the 3D case by:

$$288 \quad G(\mathbf{y}, \mathbf{x}) = -\frac{e^{ikd(\mathbf{x}, \mathbf{y})}}{4\pi d(\mathbf{x}, \mathbf{y})}. \quad (4)$$

289 Here, $d(\mathbf{x}, \mathbf{y})$ is the Euclidean distance between two points \mathbf{x} and \mathbf{y} . In Eq. 3, $\partial/\partial n$ denotes the normal derivative on the boundary
 290 (i.e., the rate of increase in the direction of the mesh's normal \mathbf{n}_m). Let $\psi(\mathbf{x}, \mathbf{y})$ denote the angle between the mesh's normal at \mathbf{y}
 291 and the vector $\mathbf{x} - \mathbf{y}$ and $\nabla_{\mathbf{y}}$ denote the gradient for the components of \mathbf{y} . The normal derivative of the Green's function at \mathbf{y} can
 292 be represented as:

$$293 \quad \frac{\partial G(\mathbf{y}, \mathbf{x})}{\partial n(\mathbf{y})} = \mathbf{n}(\mathbf{y}) \cdot \nabla_{\mathbf{y}} G(\mathbf{y}, \mathbf{x}) = \frac{e^{ikd(\mathbf{x}, \mathbf{y})}}{4\pi d(\mathbf{x}, \mathbf{y})} \left(ik - \frac{1}{d(\mathbf{x}, \mathbf{y})} \right) \cos \psi(\mathbf{x}, \mathbf{y}). \quad (5)$$

294 On the other hand, when the surface is smooth around \mathbf{x}_m , the acoustic pressure on each mesh p_m can be derived from the
 295 Helmholtz-Kirchhoff integral equation under the same impedance boundary condition (25) as:

$$296 \quad \frac{1}{2} p_m = p_m^{inc} + \sum_{\substack{m'=1 \\ m' \neq m}}^M p_{m'} s_{m'} \left[ik\beta_{m'} G(\mathbf{x}_{m'}, \mathbf{x}_m) + \frac{\partial G(\mathbf{x}_{m'}, \mathbf{x}_m)}{\partial n(\mathbf{x}_{m'})} \right]; \quad m = 1, \dots, M. \quad (6)$$

297 Eq. 6 leads a set of M linear equations to determine the M unknown pressure values at the mesh elements p_m . The equation can be
 298 represented as a simple equation system $\mathbf{A}\mathbf{p} = \mathbf{b}$, where each element of the matrix \mathbf{A} and the vector \mathbf{b} are given by:
 299

$$b_m = p_m^{inc}. \quad (7)$$

$$A_{m,m'} = \begin{cases} 0.5, & m = m' \\ -s_{m'} \left[ik\beta_{m'} G(\mathbf{x}_{m'}, \mathbf{x}_m) + \frac{\partial G(\mathbf{x}_{m'}, \mathbf{x}_m)}{\partial n(\mathbf{x}_{m'})} \right], & m \neq m' \end{cases}. \quad (8)$$

301 Once the set of pressure values at the mesh elements ($\mathbf{p} = [p_1 \ \dots \ p_M]^T$) is obtained by solving this equation system, we can
 302 compute sound pressure $p(\mathbf{x})$ at any position in the propagation field using Eq. 3. The matrix \mathbf{A} depends only on the geometry of
 303 the boundary, while the vector \mathbf{b} depends on the incident wave (i.e., direct sound contributions from the transducers). It must be
 304 noted that solving this equation takes a huge amount of time and memory for a large M .

305 **Two-step Scattering Model:** To compute the transmission matrix \mathbf{E} at high update rates, our model reformulates BEM into
 306 two parts: the set-up-related and the application-related parts. Each element of the matrix $E_{l,n}$ equals the pressure $p_{l,n}$ that the n -th
 307 transducer generates at the l -th point with a transducer's complex activation $\tau_n = 1$. In this study, we assumed $\beta_m = 0$ in Eqs. 3
 308 and 8 for all the sound-scattering surfaces used (i.e., plastic, water) because their acoustic impedances are very high when
 309 compared to air. Then, $p_{l,n}$ can be represented by using BEM as:

$$p_{l,n} = p_{l,n}^{inc} + \sum_{m=1}^M p_{m,n} s_m \frac{\partial G(\mathbf{x}_m, \mathbf{x}_l)}{\partial n(\mathbf{x}_m)}. \quad (9)$$

311 Here, $p_{l,n}^{inc}$ denotes the direct contribution from the n -th transducer to the l -th point, and $p_{m,n}$ denotes the pressure at the m -th
 312 mesh generated by the n -th transducer. Then, as shown in Fig. 2a, the transmission matrix \mathbf{E} can be represented as:

$$\mathbf{E} = \begin{bmatrix} p_{1,1} & \dots & p_{1,N} \\ \vdots & \ddots & \vdots \\ p_{L,1} & \dots & p_{L,N} \end{bmatrix} = \mathbf{F} + \mathbf{G}\mathbf{H}. \quad (10)$$

$$F_{l,n} = p_{l,n}^{inc}, G_{l,m} = s_m \frac{\partial G(\mathbf{x}_m, \mathbf{x}_l)}{\partial n(\mathbf{x}_m)}, H_{m,n} = p_{m,n}. \quad (11)$$

315 The direct incident contribution $p_{l,n}^{inc}$ can be represented as: $p_{l,n}^{inc} = P_{l,n} \Phi_{l,n}$, where $P_{l,n}$ denotes the scalar directivity of our sound
 316 sources approximated as a piston model, and $\Phi_{l,n}$ denotes the complex phase propagation approximated as a spherical sound
 317 source:

$$P_{l,n} = \frac{2J_1(kr \sin \theta(\mathbf{x}_l, \mathbf{x}_n))}{kr \sin \theta(\mathbf{x}_l, \mathbf{x}_n)} \frac{P_{ref}}{d(\mathbf{x}_l, \mathbf{x}_n)}; \Phi_{l,n} = e^{ikd(\mathbf{x}_l, \mathbf{x}_n)}. \quad (12)$$

319 Here, P_{ref} represents the transducer's reference pressure at 1 m distance; r represents the transducer's radius; $\theta(\mathbf{x}_l, \mathbf{x}_n)$ is the
 320 angle between the transducer's normal and point l ; and J_1 represents a Bessel function of the first kind.

321 As we already mentioned, we assumed $\beta_m = 0$ for all the sound-scattering surfaces in this study. The extension to other values
 322 of β_m is also possible by keeping the term of $ik\beta_{m'} G(\mathbf{x}_{m'}, \mathbf{x}_m)$ in Eq. 8 when solving the matrix \mathbf{H} and adjusting Eq. 11 to have
 323 the term when computing the matrix \mathbf{G} . We can adopt this extension, without much increasing the computational complexity.

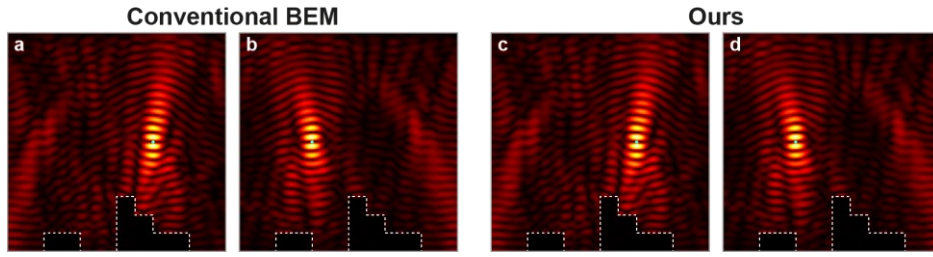
324 The important point is that the matrices \mathbf{F} and \mathbf{G} depend on point positions while the matrix \mathbf{H} , the largest and most
 325 computationally expensive element in our model, does not. Therefore, once the geometry of the set-up (i.e., transducers and
 326 scattering objects) is determined, \mathbf{H} remains constant and does not have to be computed every time we update the trapping
 327 positions (i.e., the set-up-related part). On the other hand, we must compute \mathbf{F} and \mathbf{G} every time for interactive applications (i.e.,
 328 the application-related part), but the computations of these have direct expressions given in Eq. 11 and thus are highly suitable for
 329 computing in parallel using a GPU. Therefore, once we pre-compute the matrix \mathbf{H} , the whole matrix can be computed at very high
 330 rates (see Fig. S6a). The pre-computation process for the set-up-related part to calculate the matrix \mathbf{H} is as follows:

- 331 1. Given the geometry of the sound-scattering objects, build an $M \times M$ matrix \mathbf{A} using Eq. 8.
- 332 2. Build an M vector $\mathbf{b}^{(n)}$ for the n -th transducer: $b_m^{(n)} = P_{m,n} \Phi_{m,n}$.
- 333 3. Solve $\mathbf{A}\mathbf{p}^{(n)} = \mathbf{b}^{(n)}$ to obtain $\mathbf{p}^{(n)}$ and store the results: $H_{m,n} = p_m^{(n)}$.
- 334 4. Repeat the steps 2 and 3 for all the N transducers.

335 In this study, we used a MATLAB function *gmres*, which uses the generalized minimum residual (GMRES) algorithm (40), to
 336 solve the linear systems in the step 3. An alternative way to represent the steps 2–4 is as $\mathbf{A}\mathbf{H} = \mathbf{B}$, where $\mathbf{B} = [\mathbf{b}^{(1)} \ \dots \ \mathbf{b}^{(N)}]$.
 337 We could also decompose the matrix \mathbf{A} (e.g., LU decomposition) to compute \mathbf{H} at higher speeds, instead of using GMRES.

338 **Sound-field Simulation Using Our Model:** As the conventional BEM, our model can be used for the general purpose of
 339 simulating sound fields, even though the main purpose of developing it in this study was to solve for the transducers' activation $\boldsymbol{\tau}$
 340 to create multiple traps at high speeds. Figs. S1a and S1b show the sound fields simulated by the conventional BEM (see
 341 *Conventional BEM for Scattering Problems*) when we created single traps at different positions, while Figs. S1c and S1d were
 342 simulated by our model (see *Two-step Scattering Model*) when we used the same transducers' activations $\boldsymbol{\tau}$ as Figs. S1a and S1b,
 343 respectively. In these simulations, we used the bricks object shown in Fig. S3. We can confirm that the sound fields generated by
 344 our model are equivalent to the ones simulated by the conventional BEM.

345 The conventional BEM requires solving the linear equation $\mathbf{A}\mathbf{p} = \mathbf{b}$ every time to simulate sound fields with different $\boldsymbol{\tau}$, even
 346 with the same set-up (e.g., as in the case of Figs. S1a and S1b). In contrast in our model, once we compute the transmission matrix
 347 \mathbf{E} , it can be used for simulating sound fields with different $\boldsymbol{\tau}$ unless the same set-up is used. Note here that \mathbf{E} can be computed at
 348 very high speeds (see Fig. S6a), once we obtain the data from the pre-computation (i.e., the matrix \mathbf{H}). Our model is especially
 349 useful for simulating and evaluating sound fields many times with different $\boldsymbol{\tau}$ but with the same set-up. Therefore, in this paper, we
 350 used our model for every evaluation and visualization of the sound fields.



351
352 **Fig. S1. Comparison between the conventional BEM and our two-step scattering model.** Sound fields simulated by
353 using (a, b) the conventional BEM and (c, d) our two-step scattering model when creating single traps at different
354 positions. The sound fields simulated by our model are equivalent to the ones obtained using the conventional BEM.

355 Solving for the Transducers' Phases for Acoustic 3D Manipulation

356 Once we know how to model the extended transmission matrix ($\mathbf{E} = \mathbf{F} + \mathbf{GH}$), the next step is to solve for the transducers'
357 activation $\boldsymbol{\tau}$ that generates levitation traps at target positions in the presence of sound scattering objects. In this study, we assumed
358 phase-only optimization (i.e., the amplitudes of the transducers are always maximum), and thus the goal of this optimization is to
359 find the optimum phases of the transducers ($\boldsymbol{\varphi} = [\varphi_1, \dots, \varphi_N]^T$) that maximize trapping stiffnesses $\nabla^2 U$ at every trap position \mathbf{r}_j .

360 We considered three different levitation solvers: *BASELINE*, *HEURISTIC*, and *SIMPLIFIED*. The *BASELINE* solver uses
361 stiffness, as a physically accurate and broadly accepted metric for trapping quality but is the slowest. The *HEURISTIC* solver is the
362 fastest but not accurate enough. The *SIMPLIFIED* solver represents our solutions being the most balanced, realizing accurate and
363 fast acoustic manipulation.

364 **BASELINE Levitation Solver:** One straightforward approach in this optimization problem is, as proposed in (4), to directly
365 maximize trapping stiffnesses $\nabla^2 U(\mathbf{r}_j)$ at every trap position \mathbf{r}_j by using a cost function $O(\boldsymbol{\varphi})$ determined as:

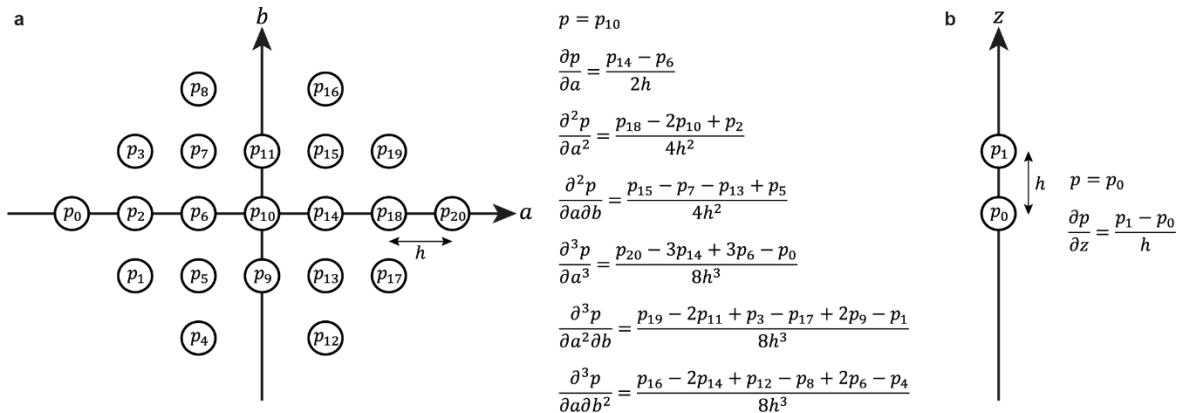
$$366 \quad O(\boldsymbol{\varphi}) = \sum_{j=1}^J \left[-\nabla^2 U(\mathbf{r}_j) + w_s (\overline{\nabla^2 U(\mathbf{r}_j)} - \nabla^2 U(\mathbf{r}_j))^2 \right]. \quad (13)$$

367 Here, the bar ($\overline{}$) represents the mean value among all the J traps; and w_s is a weight coefficient. We added the second term in this
368 cost function to equalize the qualities (i.e., stiffnesses) of all J traps by minimizing the standard deviation similarly to (41). The
369 *BASELINE* solver minimizes this cost function $O(\boldsymbol{\varphi})$ in Eq. 13 using the Broyden–Fletcher–Goldfarb–Shanno (BFGS) algorithm
370 (42, 43).

371 However, as already described in the main text, computing trapping stiffnesses $\nabla^2 U$ is computationally heavy because it
372 requires sampling pressure values at many points (e.g., 55 points in this study, which means $L = 55J$) around each trap. The
373 reason it requires so many points is that the second spatial derivative of U requires up to third derivatives of pressure values at the
374 trap position as:

$$375 \quad \frac{\partial^2 U}{\partial a^2} = 2K_1 \left(\frac{\partial p}{\partial a} \cdot \frac{\partial p}{\partial a} + p \cdot \frac{\partial^2 p}{\partial a^2} \right) - 2K_2 \sum_b^{x,y,z} \left(\frac{\partial^2 p}{\partial a \partial b} \cdot \frac{\partial^2 p}{\partial a \partial b} + \frac{\partial p}{\partial b} \cdot \frac{\partial^3 p}{\partial a^2 \partial b} \right), a \in \{x, y, z\}. \quad (14)$$

376 Here, a represents x, y , or z ; and the dot operator (\cdot) is defined as: $p_f \cdot p_g = \text{Re}[p_f] \text{Re}[p_g] + \text{Im}[p_f] \text{Im}[p_g]$. To numerically
377 obtain the derivatives in Eq. 14, this metric requires sampling pressure values at many points. In this study, we used the second-
378 order centered difference approximation to compute these derivatives for accuracy because this metric needs to serve as our
379 baseline. Fig. S2a shows how we sampled the pressure values at points around the trap in an ab -plane, where $ab \in \{xy, yz, zx\}$.
380 Note here that p_{10} in the xy -plane is duplicated in the other two planes; and p_9 and p_{11} in the xy -, yz -, and zx -planes are
381 respectively identical to p_6 and p_{14} in the yz -, zx -, and xy -planes. This means, in this study, we used 55 points in total per trap
382 (i.e., 21 for each of the xy -, yz - and zx -planes excluding the $2 + 2 \times 3 = 8$ duplicated points).
383



384 **Fig. S2. Sampling points required to compute the metrics.** (a) Sampling points in an ab -plane to calculate the trapping
385 stiffness, where $ab \in \{xy, yz, zx\}$. We used 55 points in total per trap (i.e., 21 for each of the xy -, yz - and zx -planes
386 excluding the 8 duplicated points). (b) Our proposed simplified metric requires sampling only two points per trap.
387

388 **HEURISTIC Levitation Solver:** In order to simplify this optimization problem, we adapted the heuristic approach proposed
389 in (6) for the top-bottom levitation set-ups. This approach uses two points of interest per trap (i.e., $L = 2J$), $\lambda/4$ above and $\lambda/4$

390 below the position where the trap needs to be located, with a π radian offset in the target phases. By simply back-propagating
 391 those points with the conjugate transpose of the transmission matrix \mathbf{E}^* and then constraining the transducers' amplitudes to their
 392 maxima, we can calculate the transducer phases $\boldsymbol{\varphi}$ without any iterations (i.e., $K = 1$). Although this *HEURISTIC* approach is the
 393 simplest and would work well in a single-point manipulation, destructive interference between traps is likely to occur in multi-
 394 point manipulation (15).

395 This *HEURISTIC* approach would still work even if the solver used slightly different positions for the two control points,
 396 which are at the trap position $\mathbf{r}_j = (x_j, y_j, z_j)$ and the position slightly above it $(x_j, y_j, z_j + h)$. This modified version of the
 397 *HEURISTIC* levitation solver is also used to obtain initial guesses for the *BASELINE* and *SIMPLIFIED* solvers (as explained in
 398 *Convergence and Initialization*).

399 **SIMPLIFIED Levitation Solver:** This *SIMPLIFIED* solver uses our proposed simplified Gor'kov potential U' at each trap
 400 position as our target cost function, instead of directly using trapping stiffnesses $\nabla^2 U(\mathbf{r}_j)$. As mentioned in the main text, we
 401 determined $U'(\mathbf{r}_j)$ as:

$$402 \quad U'(\mathbf{r}_j) = K_1 |p|^2 - K_2 \left| \frac{\partial p}{\partial z} \right|^2; \quad (15)$$

$$K_1 = \frac{1}{4} V \left(\frac{1}{c_0^2 \rho_0} - \frac{1}{c_p^2 \rho_p} \right); \quad K_2 = \frac{3}{4} V \left(\frac{\rho_p - \rho_0}{\omega \rho_0 (\rho_0 + 2\rho_p)} \right).$$

403 Here, V represents the volume of the levitated particle; ω represents the angular frequency; c and ρ represent the speed of sound
 404 and the density, and the subscripts 0 and p refer to the host medium (i.e., air) and the particle material, respectively. The important
 405 point here is that $U'(\mathbf{r}_j)$ can be computed by sampling pressure values at only two points around each trap (i.e., $L = 2J$, see Fig
 406 S2b), located at the trap position $\mathbf{r}_j = (x_j, y_j, z_j)$ and the position slightly above it $(x_j, y_j, z_j + h)$, in order to numerically compute
 407 the derivative along the z -axis (e.g., we used $h = \lambda/32$ in this study). Note here that adding the derivatives along the x - and y -
 408 axes (i.e., using the original Gor'kov potential shown in Eq. 1) requires sampling pressure values at four points around each trap
 409 (i.e., $L = 4J$). Our simplified metric allows about twice faster update rates when compared to using the original Gor'kov potential
 410 (described in *Computational Performance*), but (slower) solutions using the original Gor'kov potential would require minimal
 411 changes.

412 The derivative of $U'(\mathbf{r}_j)$ with respect to the phase of each transducer φ_n can be computed as:

$$413 \quad \frac{\partial U'(\mathbf{r}_j)}{\partial \varphi_n} = 2K_1 (\mathcal{I}m[p] \mathcal{R}e[p_n] - \mathcal{R}e[p] \mathcal{I}m[p_n]) - 2K_2 \left(\mathcal{I}m \left[\frac{\partial p}{\partial z} \right] \cdot \mathcal{R}e \left[\frac{\partial p_n}{\partial z} \right] - \mathcal{R}e \left[\frac{\partial p}{\partial z} \right] \cdot \mathcal{I}m \left[\frac{\partial p_n}{\partial z} \right] \right). \quad (16)$$

414 Here, $\mathcal{R}e[\]$ and $\mathcal{I}m[\]$ represent real and imaginary parts, and p_n represents a complex pressure value at the j -th trap position
 415 created by a single transducer n .

416 Due to the negative correlation between $\nabla^2 U(\mathbf{r}_j)$ and $U'(\mathbf{r}_j)$ (see Fig. 2b and explanation in section *Metric Validity*), we can
 417 obtain our cost function $O(\boldsymbol{\varphi})$ to maximize the trapping stiffnesses as:

$$418 \quad O(\boldsymbol{\varphi}) = \sum_{j=1}^J \left[U'(\mathbf{r}_j) + w_s (\overline{U'(\mathbf{r}_j)} - U'(\mathbf{r}_j))^2 \right]. \quad (17)$$

419 The weight coefficient w_s was fixed to 0.0001 in this study. The gradient of this cost function $\nabla O(\boldsymbol{\varphi})$ can be computed as:

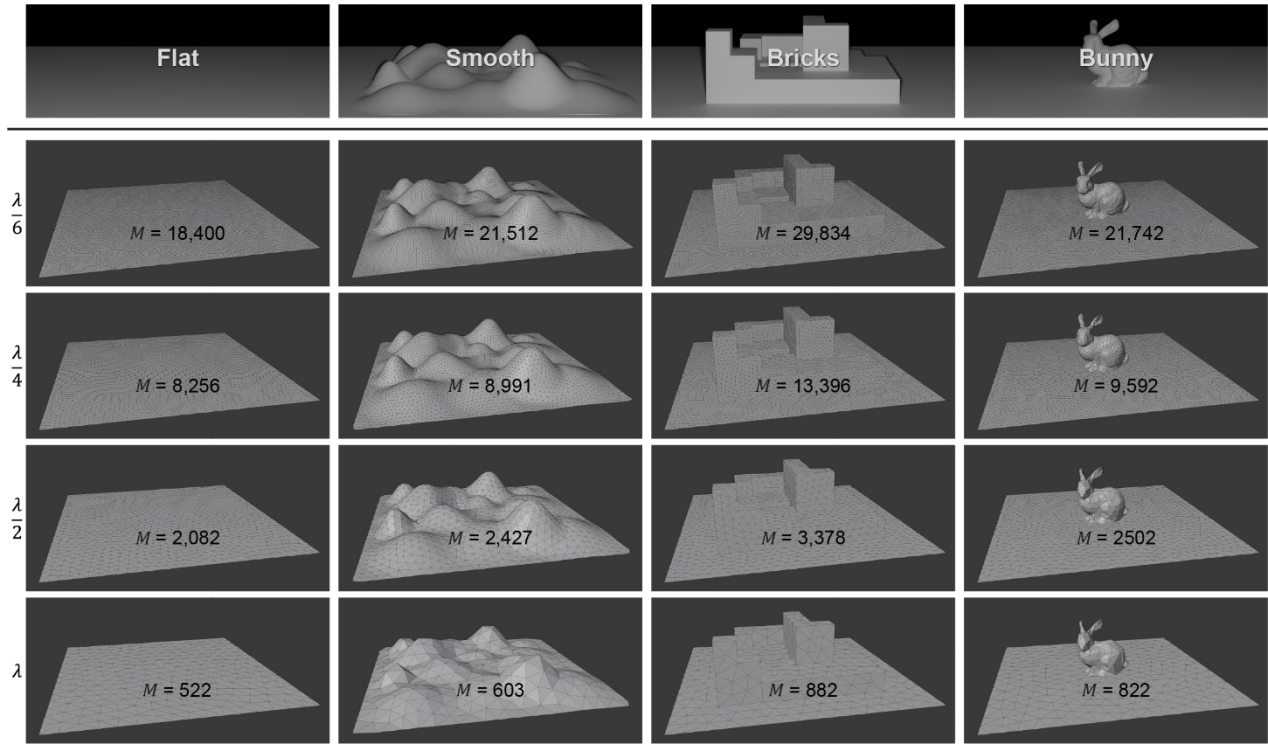
$$420 \quad \frac{\partial O(\boldsymbol{\varphi})}{\partial \varphi_n} = \sum_{j=1}^J \left[\frac{\partial U'(\mathbf{r}_j)}{\partial \varphi_n} + 2w_s (\overline{U'(\mathbf{r}_j)} - U'(\mathbf{r}_j)) \left(\frac{\partial \overline{U'(\mathbf{r}_j)}}{\partial \varphi_n} - \frac{\partial U'(\mathbf{r}_j)}{\partial \varphi_n} \right) \right]. \quad (18)$$

421 Again, computing this gradient requires sampling pressure values at only two points per trap, allowing high-speed computation.

422 Although any optimization algorithm, such as BFGS, can be used to minimize this cost function $O(\boldsymbol{\varphi})$, we decided to use
 423 gradient descent because it is suitable for parallel computation. For further simplicity, we set the step size of the gradient descent
 424 algorithm to $-1/\|\nabla O(\boldsymbol{\varphi})\|_2$, which can be determined without using any line searching algorithm. For all evaluations in this
 425 study, we set the number of iterations $K = 100$, based on the evaluation in section *Convergence and Initialization*.

426 **Evaluation of Our Acoustic Holographic Technique**

427 In this section, we describe how we evaluated our acoustic holographic technique. In the evaluations, we used four 3D models,
 428 *flat*, *smooth*, *bricks*, and *bunny*. We used a polygon mesh processing library (44) to uniformly re-mesh the 3D models so that the
 429 maximum length of the mesh elements l_{max} is always less than λ , $\lambda/2$, $\lambda/4$, or $\lambda/6$, as shown in Fig. S3. The program detects
 430 edges with dihedral angles larger than certain degrees as object features and reserves those features while re-meshing. In most of
 431 the evaluations, we used the models with $l_{max} = \lambda/2$, as it is the best-balanced mesh size between speed and accuracy (detailed in
 432 *Mesh-size Dependency of the Trap Quality*).



433
434 **Fig. S3. 3D models used for the evaluations: flat, smooth, bricks, and bunny.** The 3D models were re-meshed to have a
435 maximum length of λ , $\lambda/2$, $\lambda/4$, or $\lambda/6$.

436 **Metric Validity:** As described earlier, our *SIMPLIFIED* levitation solver uses the simplified Gor'kov potential $U'(\mathbf{r}_j)$ of Eq. 2
437 to evaluate the quality of traps, instead of using the trapping stiffness $\nabla^2 U(\mathbf{r}_j)$. To justify our choice of the metric, we evaluated
438 the correlation between $U'(\mathbf{r}_j)$ and $\nabla^2 U(\mathbf{r}_j)$. In this evaluation, the sound-scattering objects with $l_{max} = \lambda/2$ (see Fig. S3) were
439 placed at the origin $(x, y, z) = (0, 0, 0)$, and the PAT was arranged at 12 cm above the objects. We created single traps at 2,000
440 random arrangements for each of the four objects (i.e., so 8,000 samples in total). Here, the x and y coordinates of the trap
441 positions ranged from -5 to 5 cm, and z was set from 2 to 9 cm. The trap positions that were too close to the objects (i.e., the
442 distance less than 2λ) were excluded. We used the *BASELINE* solver to create the traps and computed $U'(\mathbf{r}_j)$ and $\nabla^2 U(\mathbf{r}_j)$ to plot
443 them together (see Fig. 2b). The data obtained can be linearly fit as: $U'(\mathbf{r}_j) = b_1 \nabla^2 U(\mathbf{r}_j) + b_2$ ($b_1 = -7.23 \times 10^{-7}$ and $b_2 =$
444 -1.69×10^{-8}), with the square of the correlation $R^2 = 0.940$. This correlation indicates that minimizing $U'(\mathbf{r}_j)$ would result in
445 maximizing the trapping stiffness $\nabla^2 U(\mathbf{r}_j)$.

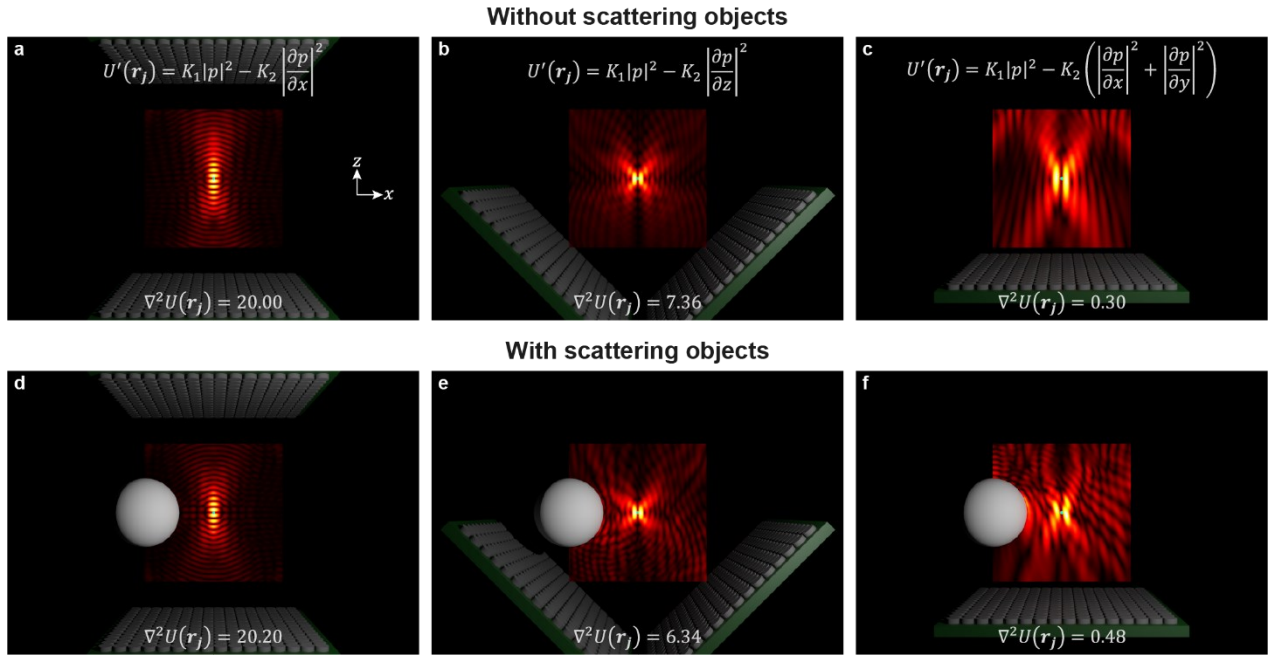
446 Although we confirmed that our simplified Gor'kov potential $U'(\mathbf{r}_j)$ can be used in our set-ups (i.e., the top array with
447 arbitrary objects), this does not necessarily apply to all experimental set-ups. Here, we demonstrate how our technique can be
448 adjusted to three other PAT set-ups: the top-bottom, V-shape, and single-sided without any reflector. Note here that we assumed
449 using the same 16×16 PAT, but the top-bottom and V-shape ones use two PATs. First, we can use the same simplification (i.e., Eq.
450 2) for the top-bottom set-up because sound waves propagating in $+z$ and $-z$ directions from the top and bottom arrays can create
451 vertical standing-wave-like traps (see Fig. S4a). In the V-shape set-up with an angle between PATs ($\phi = 90^\circ$), the propagation
452 directions of the two PATs are $(\sin \phi/2, 0, \cos \phi/2)$ and $(-\sin \phi/2, 0, \cos \phi/2)$, respectively. Therefore, thanks to the waves
453 propagating in opposite directions along the x -axis, the following metric enables the creation of strong levitation traps (see Fig.
454 S4b):

$$455 \quad U'(\mathbf{r}_j) = K_1 |p|^2 - K_2 \left| \frac{\partial p}{\partial x} \right|^2. \quad (19)$$

456 Note here that the constants K_1 and K_2 are determined by the physical properties of particles and air (see Eq. 15). The single-sided
457 set-up without any reflector is the most challenging of the three due to the absence of the sound wave propagating in the opposite
458 direction. However, we can still create a vortex trap (see Fig. S4c), which is very similar to that already demonstrated in (4), by
459 using the following metric:

$$460 \quad U'(\mathbf{r}_j) = K_1 |p|^2 - K_2 \left(\left| \frac{\partial p}{\partial x} \right|^2 + \left| \frac{\partial p}{\partial y} \right|^2 \right). \quad (20)$$

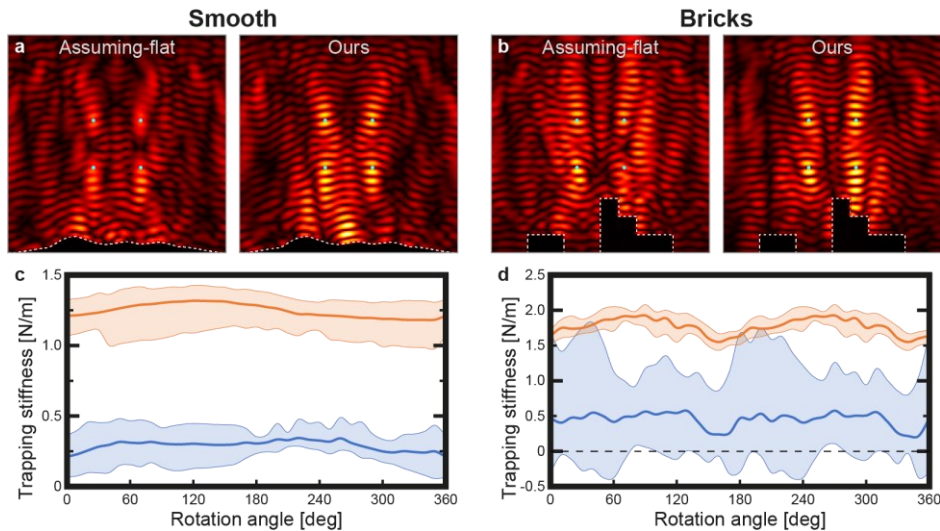
461 Our two-step scattering model works in any levitation set-up. Thus, by combining it with the levitation solver using the proper
462 metrics, we can create levitation traps with the top-bottom, V-shape, and single-sided set-ups, even in the presence of sound-
463 scattering objects (i.e., the sphere with a radius of 3 cm; see Figs. S4d, S4e, S4f).



464
465
466 **Fig. S4. Other possible metrics for different set-ups.** Creation of levitation traps with (a) top-bottom, (b) V-shape, and
467 (c) single-sided set-ups. (d, e, f) We can create traps with these set-ups even in the presence of sound-scattering objects
468 (i.e., the sphere with a radius of 3 cm). The trapping stiffness $\nabla^2 U(\mathbf{r}_j)$ in each case is shown as a reference.

468 **Distortion and Correction of Sound Fields:** To show how sound fields are distorted by sound-scattering objects and how
469 they are corrected by our two-step scattering model, we attempted to create four traps without (*assuming-flat*) and with (*ours*) our
470 model and simulated the generated sound fields. In this evaluation, we used different two 3D models (i.e., *smooth*, *bricks*) in Fig.
471 S3. As the *assuming-flat* model, we used the method of images (20). This method can compute sound waves scattering from a flat
472 reflector, by assuming them as the waves emitted by virtual sound sources located at the mirrored positions of the actual sources
473 (i.e., transducers). Therefore, these *assuming-flat* simulations do not account for sound scattering from the objects (i.e., assuming
474 there was only a flat reflector), and thus the generated sound fields can be distorted due to ignoring the presence of the objects. As
475 *ours*, we used our two-step scattering model and compared the results with the *assuming-flat* model (Figs. S5a, S5b). Then, as in
476 the surface-scanning-based display application (Fig. 4d), we horizontally rotated the trap positions and plotted the trapping
477 stiffnesses $\nabla^2 U(\mathbf{r}_j)$ at four trap points according to the rotation angle (Figs. S5c, S5d).

478 Fig. S5 shows that the sound fields are distorted a lot by both of the objects (e.g., the mean trapping stiffnesses decrease 77%
479 and 75% on average, respectively). The *bricks* object is more challenging as it has a non-smooth surface. The minimum trapping
480 stiffness with *bricks* using the *assuming-flat* model becomes even negative (Fig. S5d), suggesting at least one of the four traps is
481 not able to levitate a particle (e.g., the bottom-right trap in the *assuming-flat* image of Fig. S5b). On the other hand, our two-step
482 scattering model can correct such distortion and improve the trapping stiffness by accounting for the sound scattering from the
483 objects.

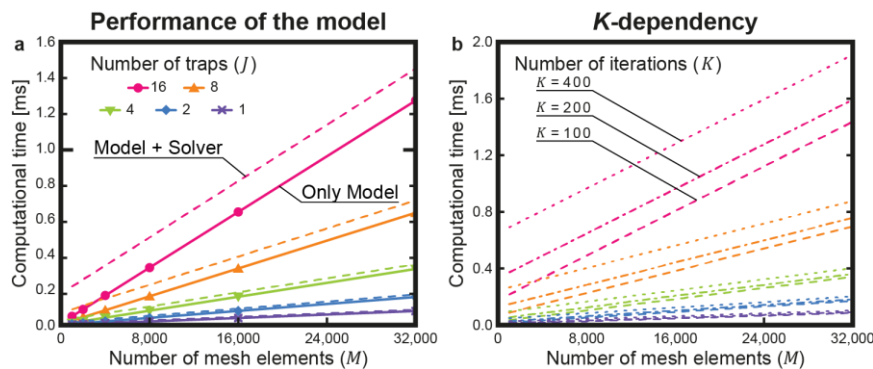


484
485 **Fig. S5. Distortion and correction of the sound fields.** (a, b) Sound-field simulations when creating four traps without
486 (*assuming-flat*) and with (*ours*) our two-step scattering model, with different 3D models (i.e., *smooth*, *bricks*). (c, d) Plots
487 showing the mean trapping stiffness of the four traps when the trap positions horizontally rotate. The shaded areas
488 represent minimum and maximum trapping stiffnesses in each case.

489 **Computational Performance:** Next, we evaluated the computational performance of our technique using a consumer-grade
 490 laptop PC (Intel Core i7-9750H CPU at 2.60 GHz) with a single GPU (NVIDIA GeForce RTX 2080). We used C++ and OpenCL
 491 for a parallelized implementation of our method. The positions of traps and mesh elements were randomly generated to be tested
 492 as the computational time does not depend on them. We tested 100 times for each combination of the numbers of traps $J =$
 493 $\{1, 2, 4, 8, 16\}$ and mesh elements $M = \{1,000, 2,000, 4,000, 8,000, 16,000, 32,000\}$, and reported the average of the
 494 computational times. Note here that in our implementation, the maximum number of frames (i.e., transducers' activation) that the
 495 GPU can compute at the same time depends on the number of workgroup size of the GPU (i.e., $N_w = 1,024$ in this case) and the
 496 number of points of interest required to compute each frame (i.e., $L = 2J$ in our solver), determined as: $N_w/2J$. This indicates the
 497 importance of choosing a metric with a small L as it directly relates to the available update rates, for example, using our simplified
 498 metric ($L = 2J$) enables the solver to compute about twice faster as using the original Gor'kov potential ($L = 4J$).

499 Figure 2c summarizes the total computational performance of our technique (i.e., the combination of our model and solver
 500 after the pre-computation), for given numbers of transducers ($N = 256$) and iterations for the solver ($K = 100$). Additionally, we
 501 tested how fast our scattering model can compute alone to show the breakdown of the computational times (see Fig. S6a). In these
 502 plots, the solid lines represent the computational time for only the model, and the dashed lines represent the total computational
 503 time (i.e., the same plots as in Fig. 2c). These plots indicate that the solving process becomes more dominant when the number of
 504 traps J is higher. This is more notable when the number of iterations K is higher (see Fig. S6b). The numbers of transducers N and
 505 traps J are determined by the hardware and applications, respectively, and thus cannot be changed. To reduce the total
 506 computational time while keeping sufficient accuracy, the numbers of mesh elements M and iterations K are keys to balancing
 507 between speed and accuracy, and we explore these next.

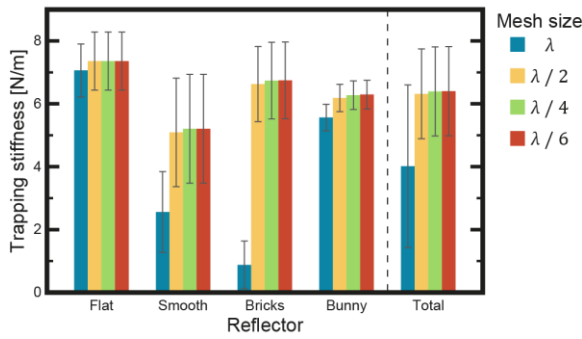
508 In these performance evaluations, we excluded the set-up-related part (i.e., pre-computation for the matrix \mathbf{H}) as our main
 509 focus is on the ability of our method to retain real-time high-computing rates for applications. Unlike the application-related part,
 510 the computational time for the set-up-related part does not depend only on N , L , and M but also on the object geometry. That is,
 511 even when two objects have the same number of mesh elements M , the computational times for these objects could differ (e.g., the
 512 *flat* reflector is easy to be solved). As references, the pre-computation for the 3D models in Fig. S3 with $l_{max} = \lambda/2$ takes about 9
 513 s for *flat*, 12 s for *smooth*, 21 s for *bricks*, and 17 s for *bunny*, using a naïve CPU implementation.



514 **Fig. S6. Computational performance in detail.** (a) Computational performance of only the scattering model (solid lines).
 515 The dashed lines represent the total computational time (i.e., model + solver excluding the pre-computation) when the
 516 number of iterations $K = 100$. (b) Total computational performance of the technique with different K .
 517

518 **Mesh-size Dependency of the Trap Quality:** As shown in Fig. 2c, the number of mesh elements M is an important parameter
 519 that highly affects the computational speed in our technique. The total number of mesh elements depends on the 3D models' mesh
 520 resolutions (i.e., the size of the elements), which also influences the accuracy of BEM. In general scattering problems using BEM,
 521 six boundary elements per wavelength are usually required for accurate scattering simulations (45). However, the purpose of this
 522 work is to solve for transducer phases that provide sufficient trapping stiffness, not to accurately simulate sound fields; therefore,
 523 such high degrees of freedom per wavelength might not be necessary for our scattering model.

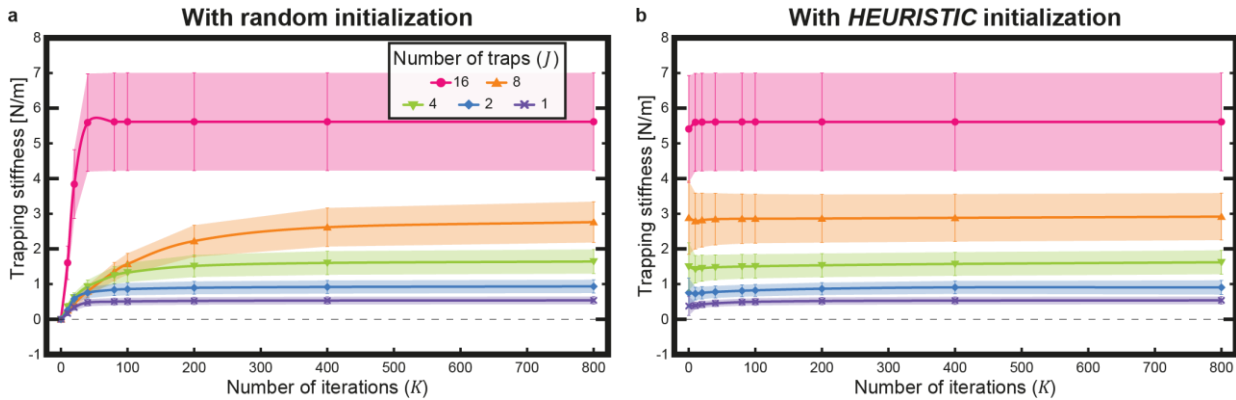
524 To find the best-balanced size for the mesh elements, we evaluated the mesh-size dependency of the trap quality (i.e., stiffness)
 525 using the 3D models in Fig. S3 with different maximum lengths of the mesh elements $l_{max} = \{\lambda, \lambda/2, \lambda/4, \lambda/6\}$. In this evaluation,
 526 we created single traps using the *BASELINE* solver at the same trap positions used in the *Metric Validity* test and then simulated
 527 the trapping stiffness $\nabla^2(r_j)$ using the finest meshes (i.e., $\lambda/6$). Figure S7 summarizes the mean stiffnesses, showing that the use
 528 of $l_{max} = \lambda$ is insufficient for our two-step scattering model, failing to provide enough stiffness (e.g., especially for *smooth* and
 529 *bricks*) compared to the subwavelength maximum element sizes. Considering the balance between speed and accuracy, we decided
 530 to use $l_{max} = \lambda/2$ in our solver for the rest of the evaluations.



531
532 **Fig. S7. Mesh-size dependency of the trap quality in our acoustic holographic technique.** When the maximum length
533 of the mesh elements $l_{max} = \lambda$, the model fails to provide enough stiffnesses at the trap positions.

534 **Convergence and Initialization:** We now show how our *SIMPLIFIED* levitation solver performs on multi-point levitation
535 (i.e., number of traps $J = \{1, 2, 4, 8, 16\}$) in the presence of the four scattering objects used in the previous evaluations (see Fig.
536 S3). We used 1,000 random combinations of trap positions per condition. To avoid cases where traps were too close to each other,
537 we set the minimum distance between the traps to 2λ . Figure S8a shows the average stiffnesses and their standard deviations with
538 different numbers of traps J , with $K = \{10, 20, 40, 80, 100, 200, 400, 800\}$, showing the increase of stiffness along with iterations,
539 when transducer phases were randomly initialized. Even with the highest number of traps (i.e., $J = 16$), we can achieve positive
540 stiffnesses, required for trapping particles, after several iterations.

541 Figure S8b shows the results when we used the phases obtained using the modified *HEURISTIC* solver instead of random
542 initial phases. The plots demonstrate that the use of such *HEURISTIC* initial guesses reduces the required number of iterations K
543 in the *SIMPLIFIED* solver. Note here that even though the *HEURISTIC* solver already provides comparatively high mean
544 stiffnesses without iterations (i.e., $K = 1$), the iterations are still required to reduce the standard deviation. This is because, in
545 multi-point acoustic levitation, weak traps could fail to hold particles in mid-air (15), and the objective is to generate equally
546 strong traps (see more discussion in the next section). The advantage of using the modified version of the *HEURISTIC* solver is
547 that it uses pressure values at exactly the same points with the *SIMPLIFIED* solver (i.e., at the trap position (x_j, y_j, z_j) and the
548 position slightly above it $(x_j, y_j, z_j + h)$) so that we can use the same transmission matrix \mathbf{E} for both these initial and iterative
549 steps, without any additional modeling process required. Following these, this *HEURISTIC* initialization and $K = 100$ were used
550 in all the applications and for the rest of the evaluations.

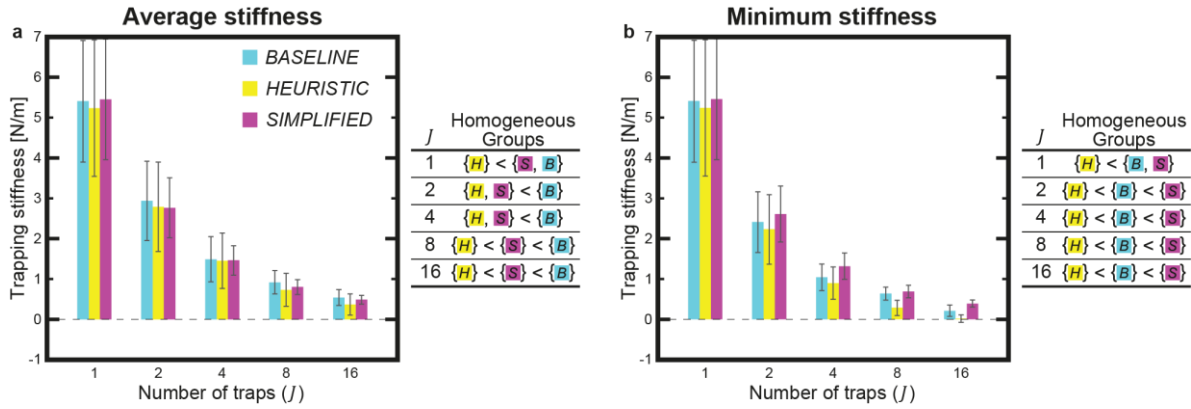


551
552 **Fig. S8. Convergence of the simplified levitation solver.** (a) The trap quality of the *SIMPLIFIED* solver improves
553 depending on the number of iterations K . (b) The use of the modified *HEURISTIC* solver as initial guesses reduces the
554 number of iterations required to be converged. The error bars represent standard deviations.

555 **Comparison between the Solvers:** In this study, we considered using three solvers: *BASELINE*, *HEURISTIC*, and
556 *SIMPLIFIED*, with our two-step scattering model. Here, we compare these three solvers to demonstrate that only the *SIMPLIFIED*
557 solver provides both high computational speed and trap quality. Similar to the previous evaluation, we used 1,000 random
558 combinations of trap positions per condition (i.e., four scattering objects with the different numbers of traps $J = \{1, 2, 4, 8, 16\}$).
559 The numbers of transducers ($N = 256$) and iterations ($K = 100$) were fixed.

560 Figure S9a shows the average trapping stiffnesses and their standard deviations obtained by the different solvers. The mean
561 values indicate that *BASELINE* overall is slightly better than *HEURISTIC* and that the performance of *SIMPLIFIED* tends to be
562 between these two. We also confirmed this relationship statistically using the statistics software (i.e., IBM SPSS Statistics 25), as
563 shown in Fig. S9a. The plots also show that *SIMPLIFIED* provides the smallest standard deviations of the solvers. Providing small
564 standard deviations is important in multi-point acoustic levitation to avoid weak traps and realize stable particle manipulation (15).

565 To highlight this point, we performed the same evaluation but focused on the weakest traps of the J traps (see Fig. S9b). The
566 plots indicate that the difference between *HEURISTIC* and the other two becomes more apparent, and *HEURISTIC* likely fails to
567 create traps when the number of traps is large (i.e., negative stiffness with $J = 16$). This is why *HEURISTIC* is not enough even
568 though it offers the fastest computational performance. Figure S9b also shows that *SIMPLIFIED* performs slightly better than even
569 *BASELINE* in terms of the minimum stiffnesses, indicating that *SIMPLIFIED* is more suitable to uniformly provide sufficient
570 stiffness for all the traps in multi-point levitation.



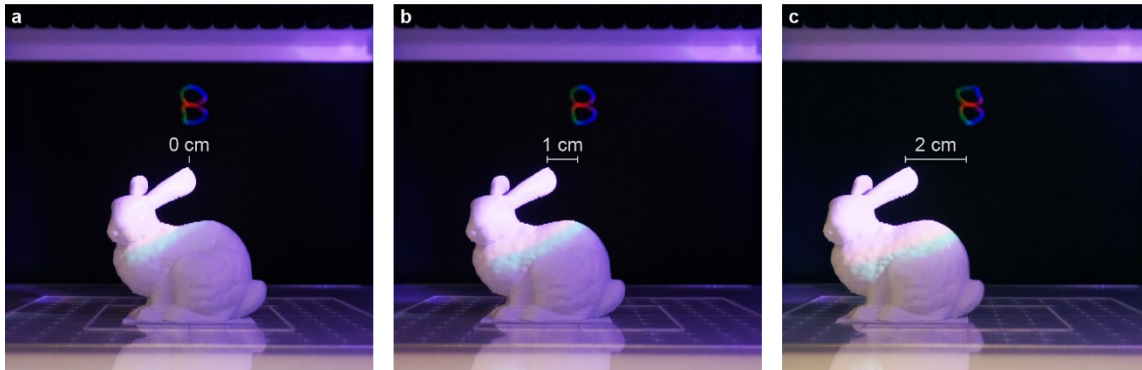
571
572 **Fig. S9. Comparison of the trap quality between the different solvers.** Average stiffnesses (a) and minimum stiffnesses
573 (b) obtained by the three different solvers. The bars represent standard deviations. The symbol ‘<’ indicates there is a
574 significant difference between the homogeneous groups represented by the symbol ‘{’.

575 **Manipulation Capability:**

576 In this section, we discuss the manipulation capabilities enabled by our technique.

577 **Moving Sound-scattering Objects:** In our scattering model, the mesh models remain static over time. This assumption allows
578 us to pre-compute the scattering model (i.e., the matrix H). In other words, dealing with dynamic scattering objects is challenging
579 in our acoustic holographic technique. If we know ahead of time the nature of the dynamic evolution of the sound scattering
580 object, different H matrices can be pre-computed, and the other two matrices F and G can be computed in real time. If the sound-
581 scattering object changes in a manner that cannot be predicted ahead of time, we need to repeatedly solve linear equations $A\mathbf{p}^{(n)} =$
582 $\mathbf{b}^{(n)}$, where A is an $M \times M$ matrix, for every N transducer to compute H in real time. Note here that, as shown in Eq. 8, the matrix
583 A depends only on the geometry of the scattering objects and not on the positions of the transducers or traps.

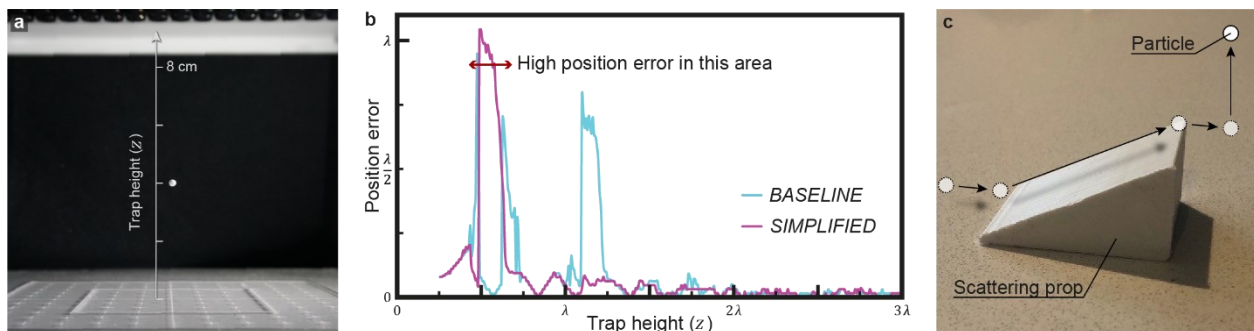
584 One common scenario is where the shape of the scattering object is constant but the object’s position or transducers’
585 arrangement changes. In such scenarios, we can assume the object is relatively static by assuming instead the positions of the
586 transducers change. Thus, the matrix A is constant even while the actual position of the object is moving. Therefore, once we
587 decompose this matrix (e.g., by using LU decomposition), we can reuse the decomposed matrices to easily solve the linear
588 equations, obtaining different H at high rates during the movement of the object. Figure S10 shows an example of creating a POV
589 image with a scattering object located at different positions. In these three examples, we used the same lower and upper triangular
590 matrices, which were obtained from the decomposition of A , to accelerate the computation of H .



591
592 **Fig. S10. Creation of POV image with a scattering object located at different locations.** (a, b, c) The center of the 3D-
593 printed bunny was located at 0, 1, and 2 cm from the center of the system, respectively.

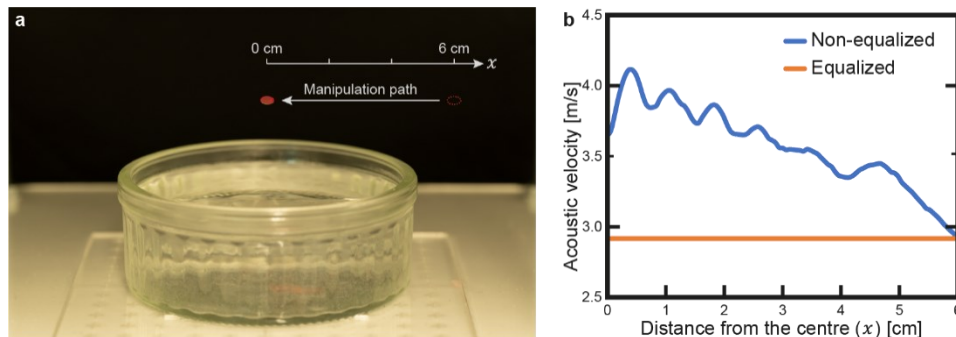
594 **Scattering Objects Vicinity:** One limitation of our technique is the manipulation of particles near the scattering surfaces.
595 When we try to create a trap near a surface, strong sound reflection from the surface tends to create standing-wave-like sound
596 fields on the surface, resulting in the creation of traps at certain discrete heights (z) from the surfaces (i.e., $z = \lambda/4, 3\lambda/4$).
597 Therefore, it is difficult to manipulate a particle from $z = \lambda/4$ to $z = 3\lambda/4$, or vice versa. To show this limitation, we tried to
598 create a single trap with our solver at certain heights (z) from the flat surface (see Fig. S11a) and plot how far the simulated trap
599 positions (i.e., positions where the Gor’kov potential is minimum) were from the target trap positions, even with the *BASELINE*
600 solver (see Fig. S11b). The plot shows very high position errors within the area around $\lambda/2 < z < 3\lambda/4$, indicating failures to
601 create the trap within this area. This manipulation difficulty near scattering surfaces was also confirmed experimentally.
602 Additional research efforts on both algorithmic and hardware fronts (e.g., transducer arrangement) are required for realizing
603 acoustic holographic systems with this feature.

604 A practical way to bypass this problem is the use of sound-scattering props (see Fig. S11c). Our two-step scattering model
605 enables us to manipulate a particle along the ramp by creating traps $\lambda/4$ over the ramp surface. Once the particle is high enough
606 from the surface (e.g., $z \geq 3\lambda/4 = 6.49$ mm), we can push the particle off the ramp and manipulate it in 3D without any
607 constraint. We have experimentally confirmed this approach works to pick up particles from the ground.



608
609 **Fig. S11. Limitation on acoustic manipulation near scattering surfaces.** (a) Experimental set-up. (b) Position error
610 near the flat surface depending on the trap height (z). Here, the wavelength $\lambda = 8.65$ mm in this study. (c) Sound-
611 scattering prop enabling to translate particles near the surface.

612 **Handling Liquid Droplets:** Consider we manipulate a liquid droplet horizontally as shown in Fig. S12a. In acoustic
613 manipulation of liquid droplets, the ratio of acoustic forces to surface forces for a levitated droplet is described by the acoustic
614 Bond number ($2, 33$) as: $B_a = 2v_{rms}^2\rho_0R_s/\sigma$, where σ is the surface tension of the liquid; R_s is the droplet radius, and v_{rms} is
615 the root mean square of the acoustic velocity of air particles. To avoid atomization of the levitated droplet (i.e., droplet bursting), this
616 acoustic Bond number needs to be between 2.5 and 3.6, as experimentally determined in (33). Therefore, it is important to keep the
617 acoustic velocity constant along manipulation paths. In our experiment, we manipulated a liquid droplet horizontally (see Fig.
618 S12a and Movie S2). The fast computational rates of our technique enable us to estimate the acoustic velocity in real time and to
619 adjust the transducers' amplitudes to make the acoustic velocity constant along the manipulation path (see Fig. 9b).



620
621 **Fig. S12. Equalization of acoustic velocity along levitation paths to avoid atomization of droplets.** (a) Definition of
622 the manipulation path of a pain droplet. (b) Adjusting the amplitudes of the transducers depending on the estimated
623 acoustic velocity (i.e., the velocity of air particles) allows the handling of liquid droplets without causing atomization.

624 MR Applications

625 In this section, we describe how we created the MR applications.

626 **Experimental Set-ups:** All our applications used the same levitation set-ups. The applications were created using a single
627 PAT of 16×16 transducers, designed as an extension of the Ultraino platform (6), modified for faster communication rates as
628 (15). The array used Murata MA40S4S transducers (40 kHz, 10.5 mm diameter ($\sim 1.2\lambda$), delivering ~ 8.1 Pa at 1-m distance when
629 driven at 20 Vpp). A Waveshare CoreEP4CE10 Field Programmable Gate Array (FPGA) board was used to receive phase and
630 amplitude updates from the CPU, using a USB FT245 Asynchronous FIFO Interface at 8 Mbyte/sec and allowing more than
631 10,000 phase and amplitude updates per second. The PAT and a base flat acrylic reflector were aligned on top of each other with
632 an adjustable separation (e.g., fixed to 12 cm in this study). A square part (12×12 cm²) of the flat reflector can be replaced by
633 arbitrary scattering surfaces, such as 3D-printed ones, sets of bricks, and a glass container filled with water. We used a LulzBot
634 mini 3D printer with eSUN PLA+ filament to 3D-print the objects. For the interactive applications (see Movie S4), we used a
635 LeapMotion sensor to detect the user's fingertip positions.

636 **Mid-air Screen:** We used the same method described in (12) to prepare the mid-air screen for levitation. We first laser-cut
637 light, acoustically transparent fabric (Super Organza) into a square of 3×3 cm². Four EPS particles were glued on the piece of
638 fabric, acting as anchors to allow 6-degrees-of-freedom manipulation of the fabric. For projection mapping onto this levitated
639 fabric, we used a projector (Texas Instruments, DLP LightCrafter Evaluation Module) with a native resolution of 608×684 pixels.
640 We obtained the intrinsic parameters of this projector in advance by using an OpenCV function (*calibrateCamera*) with a
641 checkerboard and a web camera, and then obtained the extrinsic parameters (i.e., positions and orientation, relative to the levitator
642 coordinate) by using the manually collected combinations of trap positions in the levitator coordinate and pixel positions in the
643 projector coordinate. We then used such parameters for our OpenGL cameras (i.e., projection and view matrices) to enable real-
644 time projection mapping (see Fig. 1b).

645 **Point-scanning-based Volumetric Display:** In these applications, we used high-intensity full-color LEDs (OptoSupply,
646 OSTCWBTHC1S) to illuminate the levitated EPS particles. The LEDs were directly controlled by the FPGA, which controls the
647 transducers as well so that the illumination colors and the movements of the levitated particles were synchronized. All the
648 scanning paths were generated to be scanned by the particles in the POV time (i.e., 0.1 s). Therefore, we were able to create the
649 volumetric POV images (see Figs. 4a, 4b, and 4c).

650 Note here that in the point-scanning-based approach, the maximum number of voxels N_v is determined by the update rate of
651 the levitator f_l , the number of traps J , and the POV rate ($f_{POV} = 10$ Hz) as: $N_v = J \cdot f_l / f_{POV}$ (e.g., $N_v = 4,000$ when $f_l = 10,000$
652 and $J = 4$). Also, there are additional constraints in the voxel arrangement because the paths created by these voxels need to be
653 scanned by single or multiple points. That is, the voxels need to be continuous, and the particle movements along the voxel paths
654 need to be within the system's capabilities (i.e., maximum velocity and acceleration). These constraints make it difficult to create
655 complex volumetric shapes with the point-scanning-based approach.

656 **Surface-scanning-based Volumetric Display:** We re-used the same fabric, projector, and calibration scheme used in the mid-
657 air screen application. However, in this application, we used the projector in a high-speed binary mode at 1,440 fps. As shown in
658 Fig. 4d, we placed a mirror in the system to cover the angles, where the projector is not capable of directly projecting onto the
659 fabric (i.e., when the fabric and projection direction become parallel). In other words, we used the mirror as a second projector.
660 We created 144 cross-sectional binary images of a 3D model (i.e., bunny) every 1.25 degrees, mapped those images onto the
661 rotating screen, and encoded them into 24-bit images as in (46). Then the system levitated and rotated the fabric at five rotations
662 per second while updating the encoded images at 60 Hz. Our OpenGL-based software can adjust the timing of projecting the
663 cross-sectional images so that it matches the fabric's rotational timing. The software also receives a VSYNC signal to
664 automatically adjust the timing of projecting the cross-sectional images corresponding to the levitator update.

665 In the surface-based approach, the maximum number of voxels of created images N_v is determined by the update rate of the
666 projector f_p and the number of pixels of projected 2D images N_p as: $N_v = N_p \cdot f_p / f_{POV}$. Thus, ideally, $N_v = 608 \times 684 \times 1,440 /$
667 $10 \cong 60,000,000$, which is almost 15,000 times larger than the point-based approach. Although it is not realistic to assume full
668 use of the pixels with a static projector like in our current system, it is possible to increase the usage of the pixels to nearly 100%
669 by utilizing a projection engine with a rotational mirror such as demonstrated in (39). Additionally, the voxel arrangement is
670 independent of the content because it is fixed, so the displayed content does not need to account for the levitator's capabilities (i.e.,
671 velocity and acceleration), once the levitator is able to rotate the fabric at five rotations per second.

672 References

- 673 1. M. A. B. Andrade, A. Marzo, J. C. Adamowski, Acoustic levitation in mid-air: Recent advances, challenges, and future perspectives.
674 *Appl. Phys. Lett.* **116**, 250501 (2020).
- 675 2. D. Foresti, M. Nabavi, M. Klingauf, A. Ferrari, D. Poulikakos, Acoustophoretic contactless transport and handling of matter in air. *Proc.*
676 *Natl. Acad. Sci. U. S. A.* **110**, 12549–54 (2013).
- 677 3. Y. Ochiai, T. Hoshi, J. Rekimoto, Pixie Dust: Graphics Generated by Levitated and Animated Objects in Computational Acoustic-
678 Potential Field. *ACM Trans. Graph.* **33**, 1–13 (2014).
- 679 4. A. Marzo, S. A. Seah, B. W. Drinkwater, D. R. Sahoo, B. Long, S. Subramanian, Holographic acoustic elements for manipulation of
680 levitated objects. *Nat. Commun.* **6**, 8661 (2015).
- 681 5. K. Melde, A. G. Mark, T. Qiu, P. Fischer, Holograms for acoustics. *Nature.* **537**, 518–522 (2016).
- 682 6. A. Marzo, B. W. Drinkwater, Holographic acoustic tweezers. *Proc. Natl. Acad. Sci.*, 201813047 (2018).
- 683 7. X. Ding, S. C. S. Lin, B. Kiraly, H. Yue, S. Li, I. K. Chiang, J. Shi, S. J. Benkovic, T. J. Huang, On-chip manipulation of single
684 microparticles, cells, and organisms using surface acoustic waves. *Proc. Natl. Acad. Sci. U. S. A.* **109**, 11105–11109 (2012).
- 685 8. T. Vasileiou, D. Foresti, A. Bayram, D. Poulikakos, A. Ferrari, Toward Contactless Biology: Acoustophoretic DNA Transfection. *Sci.*
686 *Rep.* **6**, 20023 (2016).
- 687 9. D. Foresti, K. T. Kroll, R. Amisshah, F. Sillani, K. A. Homan, D. Poulikakos, J. A. Lewis, Acoustophoretic printing. *Sci. Adv.* **4**, eaat1659
688 (2018).
- 689 10. T. Omirou, A. Marzo, S. A. Seah, S. Subramanian, LeviPath: Modular Acoustic Levitation for 3D Path Visualisations. *Proc. ACM*
690 *CHI'15 Conf. Hum. Factors Comput. Syst.* **1**, 309–312 (2015).
- 691 11. D. R. Sahoo, N. Takuto, A. Marzo, T. Omirou, M. Asakawa, S. Subramanian, JOLED: A Mid-Air Display Based on Electrostatic
692 Rotation of Levitated Janus Objects. *29th ACM User Interface Softw. Technol. Symp. (UIST '16)*, 437–448 (2016).
- 693 12. R. Morales, A. Marzo, S. Subramanian, D. Martínez, LeviProps: Animating Levitated Optimized Fabric Structures using Holographic
694 Acoustic Tweezers. *Proc. 32nd ACM User Interface Softw. Technol. Symp. - UIS* (2019), doi:10.1145/3332165.3347882.
- 695 13. R. Hirayama, D. Martínez Plasencia, N. Masuda, S. Subramanian, A volumetric display for visual, tactile and audio presentation using
696 acoustic trapping. *Nature.* **575**, 320–323 (2019).
- 697 14. T. Fushimi, A. Marzo, B. W. Drinkwater, T. L. Hill, Acoustophoretic volumetric displays using a fast-moving levitated particle. *Appl.*
698 *Phys. Lett.* **115**, 064101 (2019).
- 699 15. D. M. Plasencia, R. Hirayama, R. Montano-Murillo, S. Subramanian, GS-PAT: High-speed Multi-point Sound-fields for Phased Arrays
700 of Transducers. *ACM Trans. Graph.* **39** (2020), doi:0.1145/3386569.3392492.
- 701 16. V. Paneva, A. Fleig, D. M. Plasencia, T. Faulwasser, J. Müller, OptiTrap: Optimal Trap Trajectories for Acoustic Levitation Displays.
702 *ACM Trans. Graph.*, 1–25 (2022).
- 703 17. I. Sutherland, The Ultimate Display. *Proc. IFIPS Congr.* **65**, 506–508 (1965).
- 704 18. M. A. B. Andrade, N. Perez, F. Buiocchi, J. C. Adamowski, Matrix method for acoustic levitation simulation. *IEEE Trans. Ultrason.*
705 *Ferroelectr. Freq. Control.* **58**, 1674–1683 (2011).
- 706 19. M. A. B. Andrade, T. S. A. Camargo, A. Marzo, Automatic contactless injection, transportation, merging, and ejection of droplets with a
707 multifocal point acoustic levitator. *Rev. Sci. Instrum.* **89** (2018), doi:10.1063/1.5063715.
- 708 20. L. E. Kinsler, A. R. Frey, A. B. Coppens, J. V. Sanders, in *Wiley-VCH* (Princeton University Press, Princeton, 1999);
709 <http://www.degruyter.com/view/books/9781400881734/9781400881734-002/9781400881734-002.xml>.

- 710 21. T. Carter, S. A. Seah, B. Long, B. Drinkwater, S. Subramanian, UltraHaptics: Multi-point mid-air haptic feedback for touch surfaces. *UIST 2013 - Proc. 26th Annu. ACM Symp. User Interface Softw. Technol.*, 505–514 (2013).
- 711
- 712 22. B. Long, S. A. Seah, T. Carter, S. Subramanian, Rendering volumetric haptic shapes in mid-air using ultrasound. *ACM Trans. Graph.* **33**,
- 713 1–10 (2014).
- 714 23. P. Glynne-Jones, C. E. M. Démoré, C. Ye, Y. Qiu, S. Cochran, M. Hill, Array-controlled ultrasonic manipulation of particles in planar
- 715 acoustic resonator. *IEEE Trans. Ultrason. Ferroelectr. Freq. Control.* **59**, 1258–1266 (2012).
- 716 24. M. A. Norasikin, D. Martinez Plasencia, S. Polychronopoulos, G. Memoli, Y. Tokuda, S. Subramanian, SoundBender: Dynamic
- 717 Acoustic Control Behind Obstacles. *31st Annu. ACM Symp. User Interface Softw. Technol. - UIST '18*, 247–259 (2018).
- 718 25. Y. Liu, *Fast Multipole Boundary Element Method: Theory and Applications in Engineering* (Cambridge University Press, Cambridge,
- 719 2009; <http://ebooks.cambridge.org/ref/id/CBO9780511605345>).
- 720 26. S. N. Chandler-Wilde, S. Langdon, in *Unified Transform for Boundary Value Problems: Applications and Advances*, A. S. Fokas, B.
- 721 Pelloni, Eds. (SIAM, 2014), pp. 181–222.
- 722 27. S. Inoue, S. Mogami, T. Ichiyama, A. Noda, Y. Makino, H. Shinoda, Acoustic Macroscopic Rigid Body Levitation by Responsive
- 723 Boundary Hologram. *arXiv.* **328** (2017), doi:10.1121/1.5087130.
- 724 28. J. Greenhall, F. Guevara Vasquez, B. Raeymaekers, Ultrasound directed self-assembly of user-specified patterns of nanoparticles
- 725 dispersed in a fluid medium. *Appl. Phys. Lett.* **108**, 103103 (2016).
- 726 29. M. Prisbrey, J. Greenhall, F. Guevara Vasquez, B. Raeymaekers, Ultrasound directed self-assembly of three-dimensional user-specified
- 727 patterns of particles in a fluid medium. *J. Appl. Phys.* **121**, 014302 (2017).
- 728 30. T. Kozuka, K. Yasui, T. Tuziuti, A. Towata, Y. Iida, Acoustic standing-wave field for manipulation in air. *Jpn. J. Appl. Phys.* **47**, 4336–
- 729 4338 (2008).
- 730 31. H. Bruus, Acoustofluidics 7: The acoustic radiation force on small particles. *Lab Chip.* **12**, 1014–21 (2012).
- 731 32. T. Fushimi, B. W. Drinkwater, T. L. Hill, What is the ultimate capability of acoustophoretic volumetric displays? *Appl. Phys. Lett.* **116**,
- 732 244101 (2020).
- 733 33. C. P. Lee, A. V. Anilkumar, T. G. Wang, Static shape of an acoustically levitated drop with wave-drop interaction. *Phys. Fluids.* **6**,
- 734 3554–3566 (1994).
- 735 34. A. Watanabe, K. Hasegawa, Y. Abe, Contactless fluid manipulation in air: Droplet coalescence and active mixing by acoustic levitation.
- 736 *Sci. Rep.* **8**, 1–8 (2018).
- 737 35. R. W. Bowen, J. Pola, L. Matin, Visual persistence: Effects of flash luminance, duration and energy. *Vision Res.* **14**, 295–303 (1974).
- 738 36. D. E. Smalley, E. Nygaard, K. Squire, J. Van Wagoner, J. Rasmussen, S. Gneiting, K. Qaderi, J. Goodsell, W. Rogers, M. Lindsey, K.
- 739 Costner, A. Monk, M. Pearson, B. Haymore, J. Peatross, A photophoretic-trap volumetric display. *Nature.* **553**, 486–490 (2018).
- 740 37. J. Berthelot, N. Bonod, Free-space micro-graphics with electrically driven levitated light scatterers. *Opt. Lett.* **44**, 1476 (2019).
- 741 38. J. Geng, Three-dimensional display technologies. *Adv. Opt. Photonics.* **5**, 456 (2013).
- 742 39. G. E. Favalora, J. Napoli, D. M. Hall, R. K. Dorval, M. Giovinco, M. J. Richmond, W. S. Chun, 100 Million-voxel volumetric display.
- 743 *Proc. SPIE.* **4712**, 300–312 (2002).
- 744 40. Y. Saad, M. H. Schultz, GMRES: A Generalized Minimal Residual Algorithm for Solving Nonsymmetric Linear Systems. *SIAM J. Sci.*
- 745 *Stat. Comput.* **7**, 856–869 (1986).
- 746 41. S. Polychronopoulos, G. Memoli, Acoustic levitation with optimized reflective metamaterials. *Sci. Rep.* **10**, 4254 (2020).
- 747 42. Dong C. Liu, Jorge Nocedal, On the limited memory BFGS method for large scale optimization. *Math. Program.* **45**, 503–528 (1989).
- 748 43. S. G. Nash, J. Nocedal, A Numerical Study of the Limited Memory BFGS Method and the Truncated-Newton Method for Large Scale
- 749 Optimization. *SIAM J. Optim.* **1**, 358–372 (1991).
- 750 44. D. Sieger, M. Botsch, The polygon mesh processing library (2020), (available at <http://www.pmp-library.org>).
- 751 45. S. Marburg, Six boundary elements per wavelength: Is that enough? *J. Comput. Acoust.* **10**, 25–51 (2002).
- 752 46. A. Jones, I. McDowall, H. Yamada, M. Bolas, P. Debevec, Rendering for an interactive 360° light field display. *ACM Trans. Graph.* **26**,
- 753 40 (2007).

754 Acknowledgements

755 We thank E. Haynes from University College London, who helped with the supplementary videos. **Funding:** This work was

756 supported by EU's H2020 program through their ERC Advanced Grant (No. 787413) and the Royal Academy of Engineering

757 Chairs in Emerging Technology Scheme (CiET1718/14). **Author contributions:** R.H. and S.S. conceived the concept and

758 designed the research. R.H. and G.C. developed the mathematical model and solver, with contributions from D.M.P and S.S. R.H.

759 and D.M.P. implemented the algorithms and designed the software. Data analysis was led by R.H., with contributions from all

760 authors. R.H. wrote the paper, with contributions from all authors. **Competing interests:** The authors declare no competing

761 interests. **Data and materials availability:** All data needed to evaluate the conclusions in the paper are present in the paper and/or

762 the Supplementary Materials. Additional data is archived at <https://doi.org/10.5281/zenodo.6366502>.

763